DEVELOPMENT OF ION MASS SPECTROMETRY- BASED INSTRUMENTATION AND APPLICATIONS

by

Wentao Jiang

B.S., Xiamen University, 2006

Submitted to the Graduate Faculty of

The Kenneth P. Dietrich School of Arts & Sciences in partial fulfillment

of the requirements for the degree of

Master of Science

University of Pittsburgh

2014

UNIVERSITY OF PITTSBURGH

The Kenneth P. Dietrich School of Arts & Sciences

This thesis was presented

by

Wentao Jiang

It was defended on

April 17th, 2014

and approved by

Dr. Renã A. S. Robinson, Assistant Professor, Chemistry Department

Dr. Alexander Star, Associate Professor, Chemistry Department

Dr. Joseph J. Grabowski, Associate Professor, Chemistry Department

Dissertation Advisor: Dr. Renã A. S. Robinson, Assistant Professor, Chemistry Department

DEVELOPMENT OF ION MOBILITY-MASS SPECTROMETRY INSTRUMENTATION AND MASS SPECTROMETRY-BASED ANALYSIS OF DEGRADATION PRODUCTS

Wentao Jiang, M.S.

University of Pittsburgh, 2014

Ion mobility spectrometry (IMS) is a technique that can rapidly separate ions based on their mobility in an inert buffer gas and provide insights to molecular structure. When coupled with mass spectrometry (MS), IM-MS offers a powerful hybrid analytical technique that has many biological, pharmaceutical, structural, environmental and other applications. During past decades, various types of IM-MS instruments have been built and applied, of which the most popular type is IMS-time of flight (TOF) MS. However, there are biological problems which require resolution higher than TOFMS can provide. The goal of my first project was to build a drift time IMS (DTIMS) and couple it with a commercial linear ion trap (LTQ) mass analyzer which can provide not only quick separation but also mass analysis capability. It can be used for analysis of complex biochemical samples and degradation mixtures for example. Furthermore, the IMS will be subsequently transferred to a LTQ Orbitrap-Velos MS to obtain mass data with high resolution and accuracy.

The second project focuses on the analysis of carbon nanotube (CNT) and graphene oxide (GO) degradation products using MS. In recent years different methods for carbon nanomaterial degradation have been developed and it is of interest to gain better understanding of the degradation process. MS is a suitable analysis method for the detection of intermediate mixtures with mole-

cules of different molecular weight size. The objective of this project was to use MS and tandem MS data combined with other analytical techniques (e.g. nuclear magnetic resonance (NMR), Fourier transform infrared spectroscopy (FTIR)) in order to identify and determine the structures of intermediate degradation products of CNT and GO, and understand degradation mechanisms.

TABLE OF CONTENTS

LIST OF TABLES

LIST OF FIGURES

Portions of this chapter are based on the following paper:

Wentao Jiang and Renã A. S. Robinson. Ion Mobility-Mass Spectrometry. Encyclopedia of Analytical Chemistry, eds R.A. Meyers, John Wiley: Chichester. DOI: 10.1002/9780470027318.a9292.

1.0 BACKGROUND AND INTRODUCTION

This thesis works on topics concerning the development of mass spectrometry-based instrumentation and applications. There're mainly two parts included, one of which is building a hybrid drift tube ion mobility spectrometry - Orbitrap mass spectrometry instrument, and the other is the mass based analysis of the degradation products of carbon nanomaterials

1.1 PRINCIPLES OF IMS

Ion mobility spectrometry (IMS) is a powerful analytical technique that has become more widespread in the last 40-50 years. IMS has several capabilities as a stand-alone instrument and has been used to monitor the detection of atmospheric compounds[1-3], explosives[4-6], chemical warfare agents[7,8], and petrochemical reagents[3]. In recent years, IMS technology has been used to detect explosives and narcotics in airport scanner devices.

The basic principle of ion mobility separation can be simply described as a gas-phase electrophoresis technique, whereby gaseous ions are separated according to their size, shape, and charge in the presence of a weak electric field. The drift tube is filled with an inert buffer gas (i.e., argon, helium, nitrogen) at either low vacuum pressures or at atmospheric pressure conditions. Ions move according to diffusion processes through the drift tube since the energies of the ions are similar to the thermal energy of the buffer gas. Various ions will have different mobili-

ties in a given drift tube device which allows the separation of mixtures of ions and structural information to be obtained. The simplest and still major configuration of a drift tube is one in which a series of stacked ring electrodes have a static DC field applied across the electrodes and the tube is filled with an inert buffer gas. As ions move under the influence of this weakly applied electric field, they have a velocity, v_D, which is governed by the electric field, E, and mobility of the ion, K, in a specific buffer gas.

$$v_D = KE \tag{1}$$

K is measured experimentally based on the time that it takes an ion to traverse the drift tube of length, L.

$$K = \frac{L}{t_D E} \tag{2}$$

Comparisons of reduced ion mobilities, K_0, across laboratories can be obtained by normalizing for buffer gas pressure, P, and temperature, T, as follows:

$$K_0 = \frac{L}{E t_D} \frac{273}{T} \frac{P}{760} \tag{3}$$

It is often useful to deduce information about the structure (i.e., the size and shape) of specific ions based on a mobility experiment. This is possible using an experimentally derived collision cross section, Ω, for an ion which represents the average area of the molecule that interacts with the buffer gas over a range of three dimensional orientations.

$$\Omega = \frac{(18\pi)^{1/2}}{16} \frac{ze}{(k_B T)^{1/2}} \left[\frac{1}{m_I} + \frac{1}{m_B} \right]^{1/2} \frac{t_D E}{L} \frac{760}{P} \frac{T}{273} \frac{1}{N} \tag{4}$$

In the above expression, *ze* refers to the charge on the ion, k_B is Boltzmann's constant, m_I and m_B are the masses of the ion and buffer gas, respectively, and N is the number density of the buffer gas[9]. Because IMS can be coupled with MS the mass and charge of an ion can be readily deduced. By operating at specific fields (i.e., low or high) or with different pressure regimes different IMS methods can be developed.

Since the invention of IMS, various types of IMS instruments have been invented including drift time IMS (DTIMS), high-field asymmetric waveform IMS (FAIMS), aspiration IMS (AIMS) and travelling wave IMS (TWIMS). Compared to other separation techniques, IMS has advantages such as fast speed and ability to provide structural information. The typical separation time of DTIMS is on the scale of 100 ms, which is three to five orders faster than high performance liquid chromatography (HPLC) or gas chromatography (GC). Furthermore, due to the introduction of ionization methods (i.e., electrospray ionization (ESI), matrix-assisted laser desorption ionization (MALDI)) that can ionize large molecules, IMS has become a common separation method that is applicable to both small and large, volatile and non-volatile molecules.

Based on the proteomics research carried out in our group, fast separation can lead to better efficiency of analyzing complex protein and peptide samples, which means the involvement of IMS as a fast separation technique can be beneficial. This thesis describes the work of building an in-house DTIMS.

1.2 ION MOBILITY-MASS SPECTROMETRY

Although IMS has all the favorable features stated above, its relatively low resolution (i.e. ~50) limits its usage as a stand-alone technique [2]. To achieve high resolving power and high accuracy, mass spectrometry (MS) is an ideal choice. MS plays a very important role in the identification of species in fields such as proteomics, metabolomics, lipidomics and so on. The resolving power of MS can go as high as 2×10^7.[10] The fact that both IMS and MS analyze ions in the gas phase facilitates the coupling of these two techniques. Hybrid IM-MS instrumentation significantly extends the potential applications and therefore has been an active research area in past decades[11-13].

IM-MS began with the work performed by McDaniel in the late 1950s and 60s when he developed an IM-MS instrument to study ion molecule reactions of noble gases and pure hydrogen[14]. His instrument design was a low pressure drift device that was coupled to a magnetic sector mass spectrometer. Kebarle also created an early IM-MS device for measuring ethylene gaseous ions[15]. Over the last 40 to 50 years, there have been numerous developments in IM-MS devices. The basic components found in any IM-MS instrument include the source, drift tube, mass analyzer, focusing elements, and ion detector. Technological advances in each of these components have greatly added to the overall improvement of IM-MS instruments. Different combinations of IMS and MS instruments have been realized, including IMS-time of flight mass spectrometers (TOF MS) [16-18], IMS-quadrupole mass spectrometers (qMS) [19-21], IMS- ion trap mass spectrometers (IT MS) [22-24], IMS-Fourier transform mass spectrometers (FTMS) [10,25], and IMS-magnetic sector mass spectrometers[14].

Within all these combinations, IMS-TOF MS is the most rapid IM-MS technique as a typical TOF scan only takes tens of μs. An ion gate is not necessary for IMS-TOF MS. However, the resolution of TOF is limited[26]. Except TOF MS, all other types of MS coupled with DTIMS need to apply ion gates, so the analysis speed is sacrificed. FT ion cyclotron (FTICR) MS can provide extremely high resolution which far more exceeds TOF MS. However, it also requires strong magnetic fields and cryogen which are very expensive to maintain. For the studies of large molecules, an IM-MS with a high resolution and easy MS setup is useful.

Based on the facts stated above, the goal of the project was to build a DTIMS-Orbitrap MS instrument, in order to satisfy the demands of faster separation and high resolution in our proteomics research. In this thesis, the design of the DTIMS, including ion source, drift tube, focusing lenses and interface to commercial MS, vacuum system and electronics system are described.

1.3 CARBON NANOMATERIAL AND ITS DEGRADATION

In recent years the research of carbon nanomaterials has attracted a lot of attention[27,28]. Carbon nanotubes (CNTs) and graphene are especially of interest. CNTs are allotropes of carbon with a cylindrical nanostructure. CNTs can be categorized as single-walled carbon nanotubes (SWNTs) and Multi-walled carbon nanotubes (MWNTs). Graphene is another allotrope of carbon which is a single atomic layer of graphite. It has a 2D structure formed by sp^2 hybridized carbon atoms. The CNT and graphene are related since we can take the CNT as rolled graphene sheets.

Novel properties have been demonstrated from those carbon nanomaterials including thermal, mechanical, electrical, optical properties and others[29-32]. The applications of these nanomaterials have extended to biological and biomedical areas such as drug delivery[33-36] and biosensing[37,38].

While a lot of effort has been made on biomedical applications of carbon nanomaterials, relatively less attention has been focused on degradation mechanisms. Carbon materials have biotoxicity which can lead to unusual and robust inflammatory response, oxidative stress and formation of free radicals and accumulation of peroxidative products[39-41]. These results urge the development of mild and bio-compatible methods of carbon material degradation and research of degradation mechanisms.

The goal of the project of carbon material degradation product analysis is to elucidate the degradation mechanisms of different degradation system. Since the intermediates can be small molecules, the use of MS is one of the best choices. By the interpretation of MS and MS/MS, we aimed at getting the structures of intermediates, and thereafter understand the mechanisms. In this thesis, the analysis of three degradation systems were studied, including the degradation of CNTs by strong acid or H_2O_2 under the function of enzymes, and the degradation of graphene oxide through Photo-Fenton reaction.

Portions of this chapter are based on the following paper:

Wentao Jiang and Renã A. S. Robinson. Ion Mobility-Mass Spectrometry. Encyclopedia of Analytical Chemistry, eds R.A. Meyers, John Wiley: Chichester. DOI: 10.1002/9780470027318.a9292.

2.0: DEVELOPMENT OF ION MOBILITY-MASS SPECTROMETRY INSTRUMENTATION

2.1 INTRODUCTION

DTIMS-MS is the most widespread developed and employed IM-MS approach. DTIMS is the only IMS method which provides a direct measure of collision cross section based on an ion's mobility [42]. Figure 1 shows a simple drift tube instrument that is filled with inert buffer gas in a counter direction of the ion motion. The weak electric field applied to the drift tube is generated using a series of resistors and a DC potential. The electric field applied is generally around 2.5-20 $V \cdot cm^{-1}$ [43,44] in reduced-pressure IMS (i.e., the drift pressure ranges from 1-15 mbar). Higher voltages are applied across the drift tube when higher pressures, such as atmospheric pressures, are used[22,45]. Regardless of the pressure regime used, it is important that the voltages applied do not cause the potential breakdown of the buffer gas. Traditionally used buffer gases are helium, nitrogen, and argon or mixtures thereof[17,42,46-49].

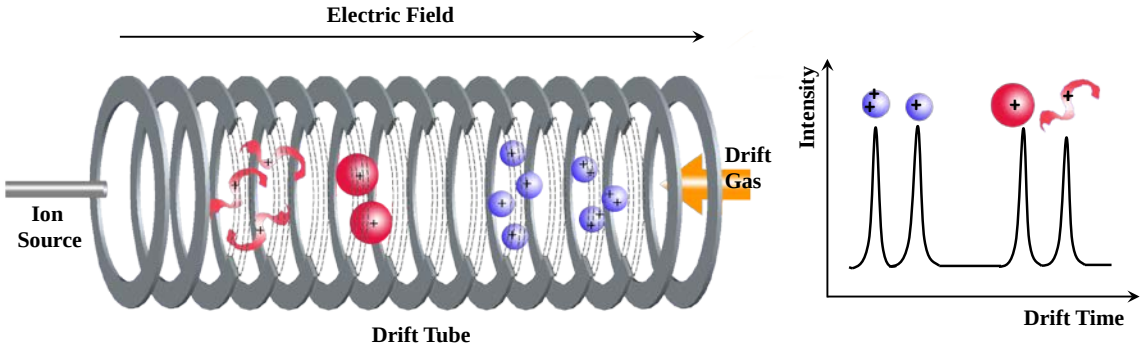

Figure 1. Principle of DTIMS. Packets of ions are injected into a drift tube filled with an inert buffer gas. Under the influence of a weak electric field, ions are separated by charge, size, and shape.

As DTIMS separates packets of ions, when continuous ionization methods are applied, an ion gate[16,45] or ion funnel[43,50] is needed to introduce packets of ions into the drift tube. Ion packets can range in width from 100-200 μs. Because of the use of ion packets, the overall sensitivity of the method is reduced[51] such that only 0.1-1% of ESI generated ions are sent to the IMS. After the ions are injected into the drift tube, the species begin to separate based on their mobility through the buffer gas. For example, doubly-charged species experience the force of the electric field twice as much as singly-charged ions, therefore for ions of the same shape the doubly-charged ion will have a higher mobility through the tube and thus a shorter drift time. Also, ions which have more elongated conformations will undergo more collisions with buffer gas atoms and thus take a longer time to drift through the tube than more compact structures. These concepts are illustrated in Figure 1.

Typically, ions travel through the drift tube on the order of milliseconds[52] which makes for a relatively fast separation. As can be inferred from the mobility equations above (see Chapter 1), the length of the drift tube can influence the transient time and mobility of an ion. The drift resolving power ($t/\Delta t$) at full-width half maximum is approximated as follows:

$$\frac{t}{\Delta t} \approx \left(\frac{LEze}{16 k_B T \ln 2} \right)^{1/2} \quad (5)$$

This theoretical resolving power approximation[53] shows that increasing the length of the drift tube or applied electric fields, or decreasing the buffer gas temperature can increase the resolving power. A typical length for an custom built IMS drift tube is ~1 meter. Clemmer[54] and Bowers[55] have shown that increasing the tube length to 2 meters or greater can significantly improve the resolving power. A circular drift tube design, which has effectively infinite length, can extend the drift resolving powers of small peptides to >300 [56]. Cryogenically cooled drift tubes with subambient temperatures have been recently demonstrated[57]. The ability to work with higher resolution drift instruments allows greater separation power for complex mixtures or isomeric and isobaric species with closely-related mobilities and can give better insight into structural transitions in the gas-phase.

2.2 DEVELOPMENT OF DTIMS – LTQ MS INSTRUMENT

LTQ MS is a commercial MS instrument with a linear ion trap mass analyzer. The setup of LTQ MS is shown in Figure 2. It consists of an atmospheric interface which can be coupled with ESI or nano ESI ion source, multipole ion guides and linear ion trap. The ion trap can carry out tandem MS for ions of interest.

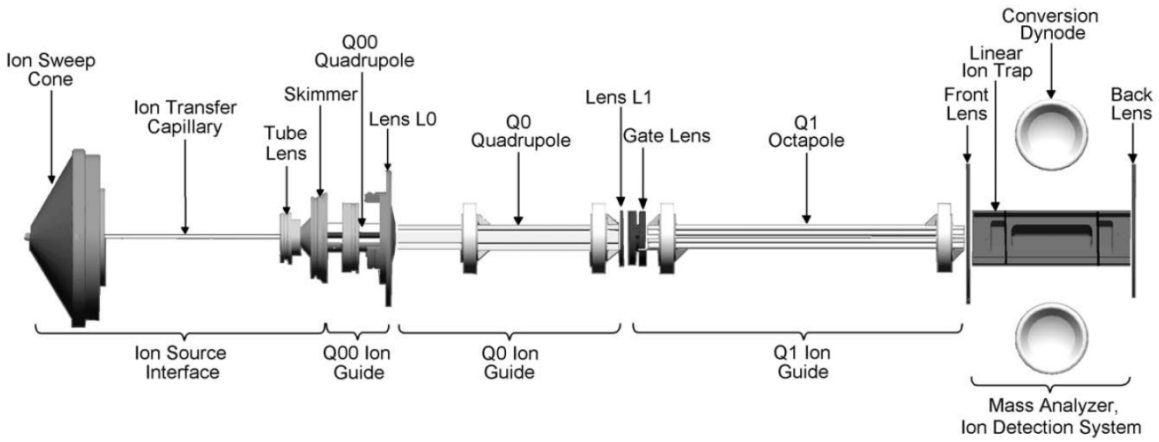

Figure 2. A schematic of Thermo LTQ MS instrument. Taken from LTQ Hardware Manual. Copyright 2003 Thermo Electron Corporation.

Recently a DTIMS-LTQ Velos MS instrument has been reported which uses photodissociation fragmentation of ions trapped in the LTQ[24]. Here, we construct a DTIMS-LTQ MS with the emphasis on ultimately obtaining high resolution MS detection with an Orbitrap MS. The proposed DTIMS-Orbitrap MS will have high resolution and high mass accuracy, relatively fast separations and MS^n capabilities.

This thesis describes the construction of an in-house DTIMS, including the drift tube, the electronic system and the vacuum system based on a previously reported instrument[58]. Also we describe the design of an interface to couple the DTIMS to the commercial LTQ MS to obtain a hybrid instrument.

2.3 EXPERIMENTAL

2.3.1 Overview of the IM-MS Instrumentation

The proposed IM-MS instrument is shown in Figure 2. The design of the DTIMS originated from Clemmer and coworkers[58]. The setup comprises an ESI ion source, source chamber, drift tube, back funnel and LTQ MS (Thermo Electron, San Jose, CA, USA). There are two funnels and three ion gates used in this instrument. An overview of the principle is as follows. Ions are generated by ESI and transferred through the capillary centered at the source block into the vacuum chamber. An hourglass funnel (based on Smith's design[50]) accommodated in the source chamber is used to trap and focus incoming ions. The lens after the hourglass funnel is the first ion gate (G1) which pulses ions into the drift tube. The widened part of the hourglass funnel enlarges the space (~6 cm^3) for accumulating and storing ions for each pulse. When the potential of G1 is lowered the ion packet is sent into the drift region. Different ions are separated while travelling through the drift tube and reach the second ion gate (G2) located before the back funnel. For each IMS separation cycle, G2 only opens for a short time window (e.g., 0.1 μs) to select ions with a specific drift time. This is realized by opening G2 with a different delay time in reference to the open time point of G1. Ions that pass G2 would be focused in the back funnel and ejected into the entrance of the LTQ MS instrument to be analyzed.

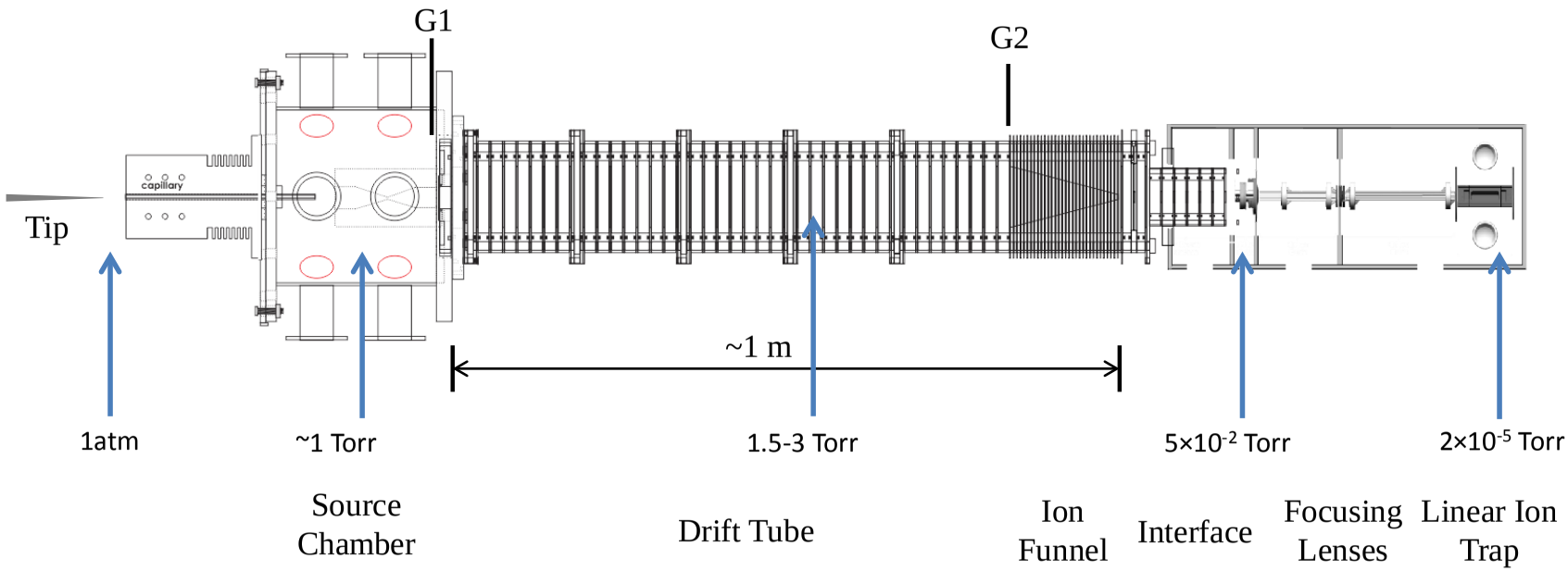

Figure 3. Schematic of the DTIMS-LTQ MS instrument. It consists of an ESI source, ~1 m drift tube, and linear ion trap.

2.3.2 Ion Source and Source Chamber

An ESI source is used for the instrument. A source block made of alumina is used as shown in Figure 3. The source block is aligned and fixed to the chamber mounting plate and sealed with O-rings. The chamber mounting plate covers and seals the front end of the source chamber. A 7.500” long capillary with a centered hole of 0.0625” serves as the path conducting the ions generated by ESI at atmosphere pressure into the vacuum source chamber. Before entering the capillary, ions will pass a 0.030” orifice of a BeCu plate located before the capillary. Ions will be sprayed out from a fused silica tip with 100 µm inner diameter held by a linear XYZ stage with 1.0” translation distance on each axis. Note that there are six slots distributed on both sides of the capillary which can accommodate cartridge heaters for higher source temperature if necessary.

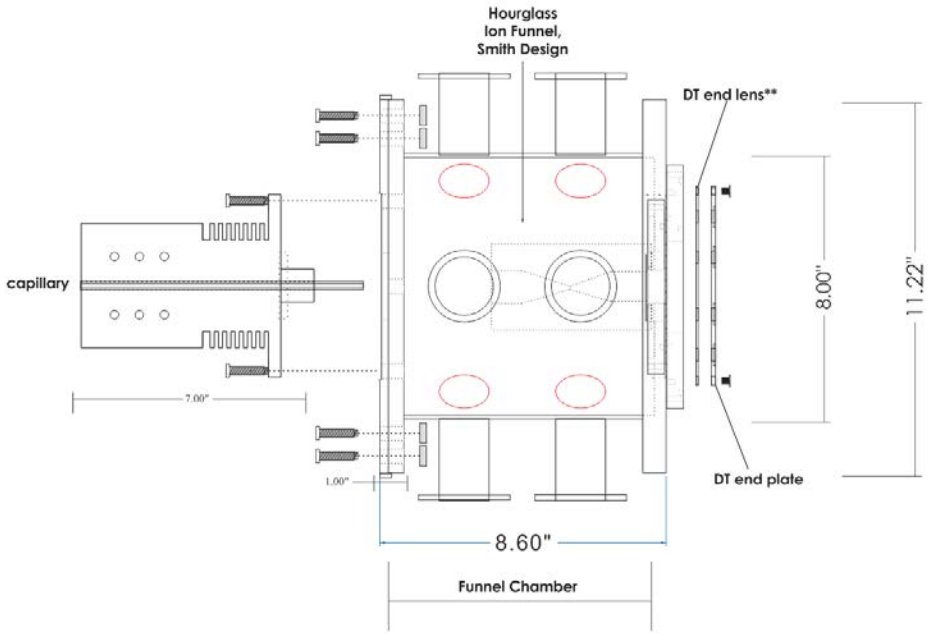

Figure 4. Schematic showing the setup of source block and source chamber. Six CF flanges and four KF flanges are distributed on the wall of the chamber as shown. The hourglass funnel is accommodated in the chamber.

As shown in Figure 4, the 8.35” long cylindrical source chamber is machined with an 8.00” O.D. and 0.125” wall thick stainless steel tube welded with a 0.70” thick drift tube mount-

ing plate. The source chamber has six KF-flange ports for pumping and four CF-flange ports for electrical connections from outside to inside of the chamber. The pressure in the chamber will be maintained at ~1 Torr. Four mechanical pumps are used to maintain the vacuum of the chamber (one Alcatel 2063, 17.9 L/s and three Alcatel 2033, 8.9 L/s). At this stage, only two CF flanges are used for electric connection while the other two are sealed with blank CF flanges. A CF flange with eight DC feedthroughs is used for all DC connections with lenses inside the chamber, and a flange with two MHV feedthroughs is used for RF potentials needed to operate the hour-glass funnel (HGF) which will be described later. Ion lenses accommodated in this chamber include the HGF, the first ion gate lens, and the first and second drift lenses.

2.3.3 Drift Tube

The drift tube is constructed by stacking 0.0625” thick stainless steel ring lenses with constant 2.750” apertures and 0.500” thick Delrin insulation spacers. For easier assembling and better flexibility of drift region length, small sections of 4.25” length were designed and assembled before the assembling of the whole drift tube. Each section has eight drift lenses and two end flanges. For each section, drift lenses and Delrin spacers, with O-rings in between, are aligned and compressed with eight threaded nylon rods and nylon nuts. Different sections are connected with modified Delrin spacers and O-rings (Figure 5). The whole drift tube forms a 2.75” path for ions to be transmitted.

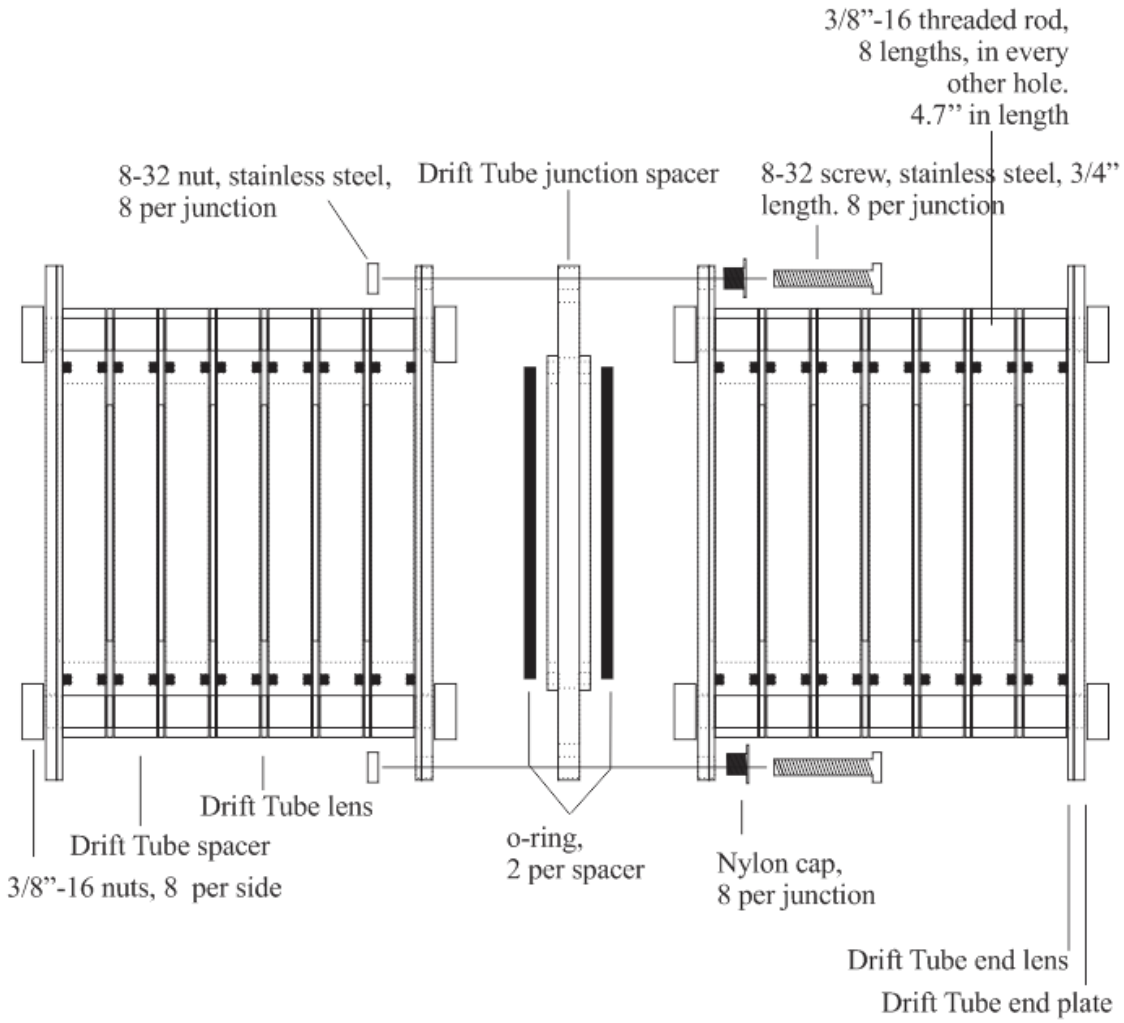

Figure 5. Schematic of drift tube sections and the modified spacer in between. Revised from Koeniger et al. Analytical Chemistry 2006, 78, 4161. Copyright 2006 American Chemical Society.

Adjacent drift lenses are connected with resistors which have 5 MΩ resistance and 1% tolerance (Newark, Gaffney, SC). The resistor chain formed can generate a nearly homogeneous DC electric field pointing from the chamber to the back funnel when connecting the first and last drift lenses to positive end and negative end of a high voltage DC power supply. The drift tube will be filled with helium at 1.5-3 Torr flowing from the end of the tube towards the source

chamber as the drift gas. The inlet of He is located behind the back funnel and connected to a cylinder through a variable leak valve (Brooks Automation, Inc.).

2.3.4 Funnels

This instrument uses two funnels to focus ions entering and exiting the drift tube.

The HGF set has 96 lenses with different aperture sizes. Those lenses are made of 0.020” thick square brass plates with tabs. Adjacent lenses are insulated by two pieces of 0.015" thick Teflon film. All the lenses are aligned and compressed by having four ceramic tubes running though the 0.25” holes at each corner of the lenses. Four threaded rods go through the ceramic tubing and fix the funnel onto a Delrin HGF mounting plate. Note that G1 and the first drift lens is at the end of this assembly. The sizes of the funnel lens apertures are listed in Table 1. Figure 6 is a schematic of the profile formed by the lens apertures. Lenses of section 1 and section 4 have constant aperture diameter, while lenses of section 2 and section 3 have decreasing and increasing aperture diameters respectively. All four sections form an hourglass profile as shown.

Table 1. The diameters of the hourglass funnel lens apertures.

	Number	Aperture(")		Number	Aperture(")		Number	Aperture(")		Number	Aperture(")
Section 1	1	1.000	Section 2	25	0.933	Section 2	49	0.409	Section 3	73	0.319
	2	1.000		26	0.913		50	0.386		74	0.346
	3	1.000		27	0.890		51	0.362		75	0.378
	4	1.000		28	0.870		52	0.343		76	0.406
	5	1.000		29	0.846		53	0.319		77	0.433
	6	1.000		30	0.823		54	0.299		78	0.465
	7	1.000		31	0.803		55	0.276		79	0.492
	8	1.000		32	0.780		56	0.256		80	0.524
	9	1.000		33	0.760		57	0.232		81	0.551
	10	1.000		34	0.736		58	0.209		82	0.583
	11	1.000		35	0.717		59	0.189		83	0.610
	12	1.000		36	0.693		60	0.165		84	0.642
	13	1.000		37	0.669		61	0.146		85	0.669
	14	1.000		38	0.650		62	0.122		86	0.697
	15	1.000		39	0.626		63	0.102		87	0.728
	16	1.000		40	0.606		64	0.079		88	0.756
	17	1.000		41	0.583	Section 3	65	0.083	Section 4	89	0.787
	18	1.000		42	0.563		66	0.110		90	0.787
	19	1.000		43	0.539		67	0.142		91	0.787
	20	1.000		44	0.516		68	0.169		92	0.787
	21	1.000		45	0.496		69	0.201		93	0.787
	22	1.000		46	0.472		70	0.228		94	0.787
	23	0.976		47	0.453		71	0.260		95	0.787
	24	0.957		48	0.429		72	0.287		96	0.787

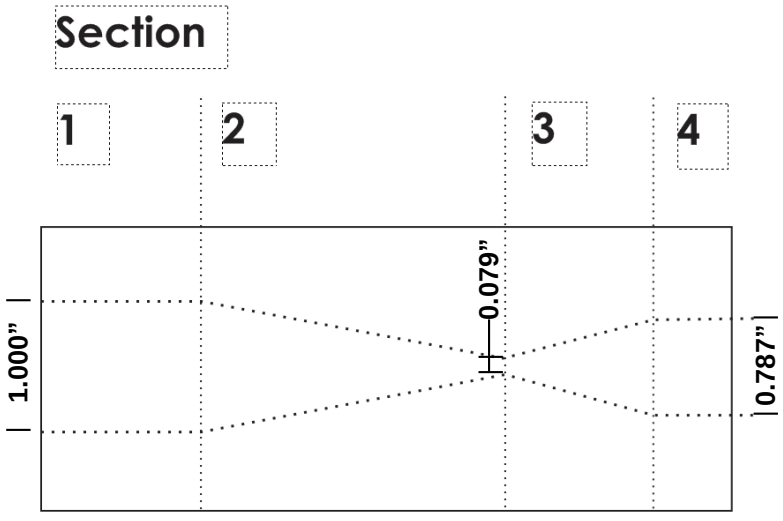

Figure 6. The profile formed by HGF lens apertures

In addition to a resistor chain used for the DC electric field, capacitors are involved to generate an RF field. All even number lenses are connected to one end of a RF generator through capacitors, while lenses with odd numbers are connected to the other end. The simplified diagram of a funnel is presented in Figure 7(a). The electrical connections for the HGF are realized using two printed boards with ZIF sockets (3M, Austin, TX). Each board is in charge of half the number of lenses with the circuit shown in Figure 7(b). Connection tabs for adjacent funnel lenses are staggered in order to fit into two ZIF sockets. Dots shown in Figure 7(b) are the spots where funnel lenses are connected to the Zif sockets. 1 MΩ (0.1%, 15ppm) resistors and 1000 pF (10%) capacitors are used. According to published reports, an effective electric field for ion transfer can be generated with 11 V/cm and 50-70 V_{p-p} (450kHz)[44].

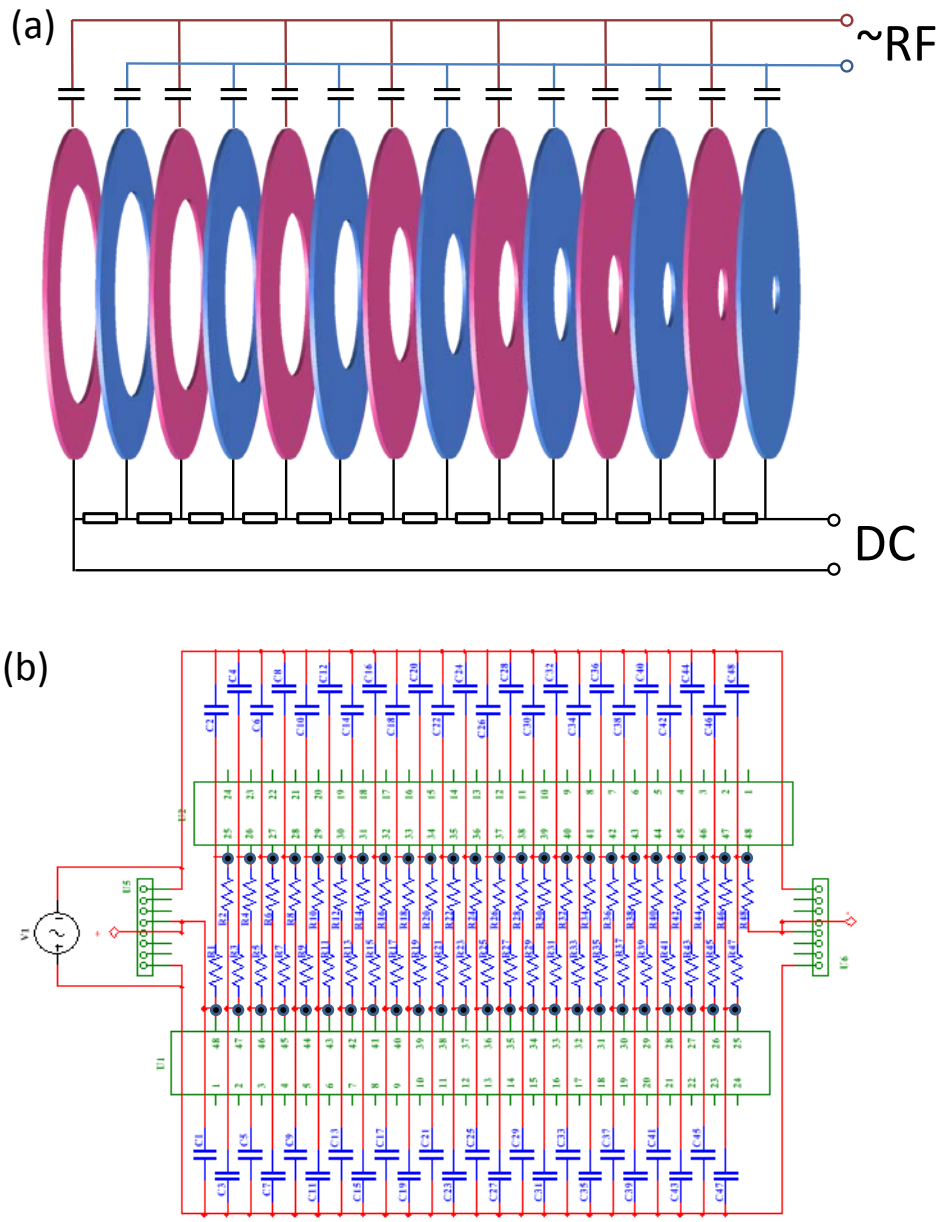

Figure 7. (a) The illustration of resistors and capacitors connected to funnel lenses. (b) The printed board circuit for HGF lens electronic connections.

Similar construction is used with the back funnel. The back funnel has 30 lenses that are made of 0.0625” thick stainless steel with aperture diameters decreasing from 69.93 mm to 7.76 mm linearly. Delrin spacers (0.125” thick) and O-rings are used to space and seal the back funnel

lenses. Eight nylon threaded rods and nuts are used to compress the funnel. Lenses are connected to 5MΩ (0.1%) resistors and 500 pF (10%) capacitors. The total length of the back funnel is 5.3". Tentative potentials that will be applied are ~10 V/cm and 70-100 V_{p-p} (~450 kHz)[44].

2.3.5 Ion Gates

Two ion gates are made by covering lens apertures by spot welding a piece of nickel mesh (70 lpi, 5 μm, Precision Eforming) onto it. A bias voltage of ~50 V applied to the ion gate can usually can confine ions before the gate and lowering the bias to ~-20 V can eject the ions[24].

G1 is placed right after the last HGF electrode with 1.84 mm spacing which is operated as a pulsing lens that sends ion packets into the drift tube. It is connected with a pulse generator that can generate ~100 μs potential pulses with changeable frequency. At the time the pulses are generated, the potential of G1 is lowered to -20 V, which is maintained to be 50 V otherwise. The opening of G2 is triggered by action of G1. A variable time delay is needed depending on the drift time window to be selected. For ions, they are confined by G1 and stored in the HGF till the G1 pulse happens. Most ions are lost except those which have a drift time the same as the time delay of G2. The principle is illustrated in Figure 8. By scanning the delay time of G2, ions of each time window will be sent into the LTQ MS, which will generate an entire IMS spectrum.

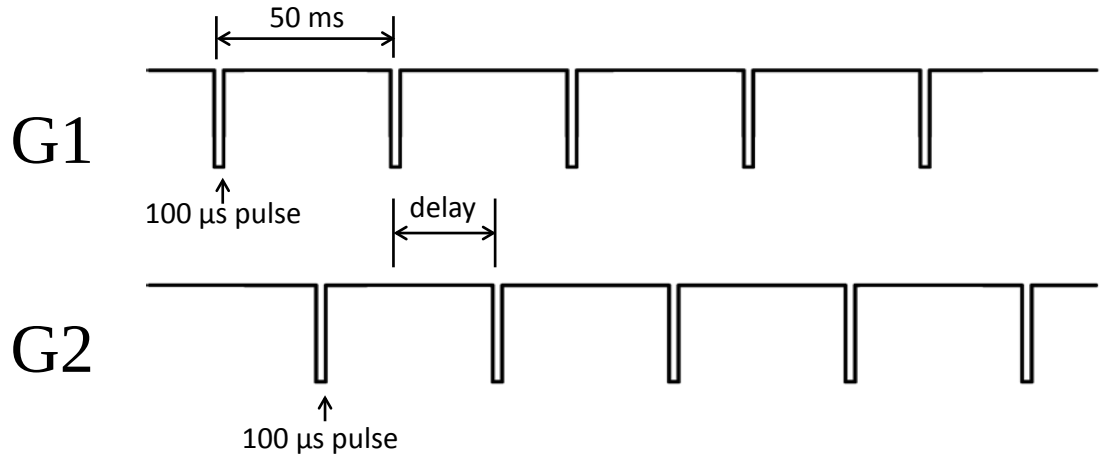

Figure 8. Example of a pulsing diagram for a dual gate DTIMS-LTQ MS experiment. The upper trace shows that an ion packet (100 µs width) is injected into the drift tube by G1 and mobility separated over the course of 50 ms. The lower trace shows G2 opens after a variable time delay trigered by G1 pulses to select ions with certain drift time.

It should be noted that for the future action of coupling the IMS to the Orbitrap MS, a third ion gate will be constructed after the back funnel to store ions before injecting them into the MS. This is necessary since the high resolution scan (e.g. 100K) of the Orbitrap takes around 1 s which is an order of magnitude longer than the IMS separation.

2.3.6 IM-MS interface

To transfer the ions exiting the back funnel efficiently into the commercial MS instrument, the original atmospheric pressure-MS interface needs to be revised to match both the pressure and electric field to the end of drift tube. A tentative interface has been designed and is shown in Figure 9(a). The drift gas inlet plate is accommodated at the end of the back funnel. Then smaller drift tube lenses are used in order to guide ions into the entrance of the MS. For the MS, the

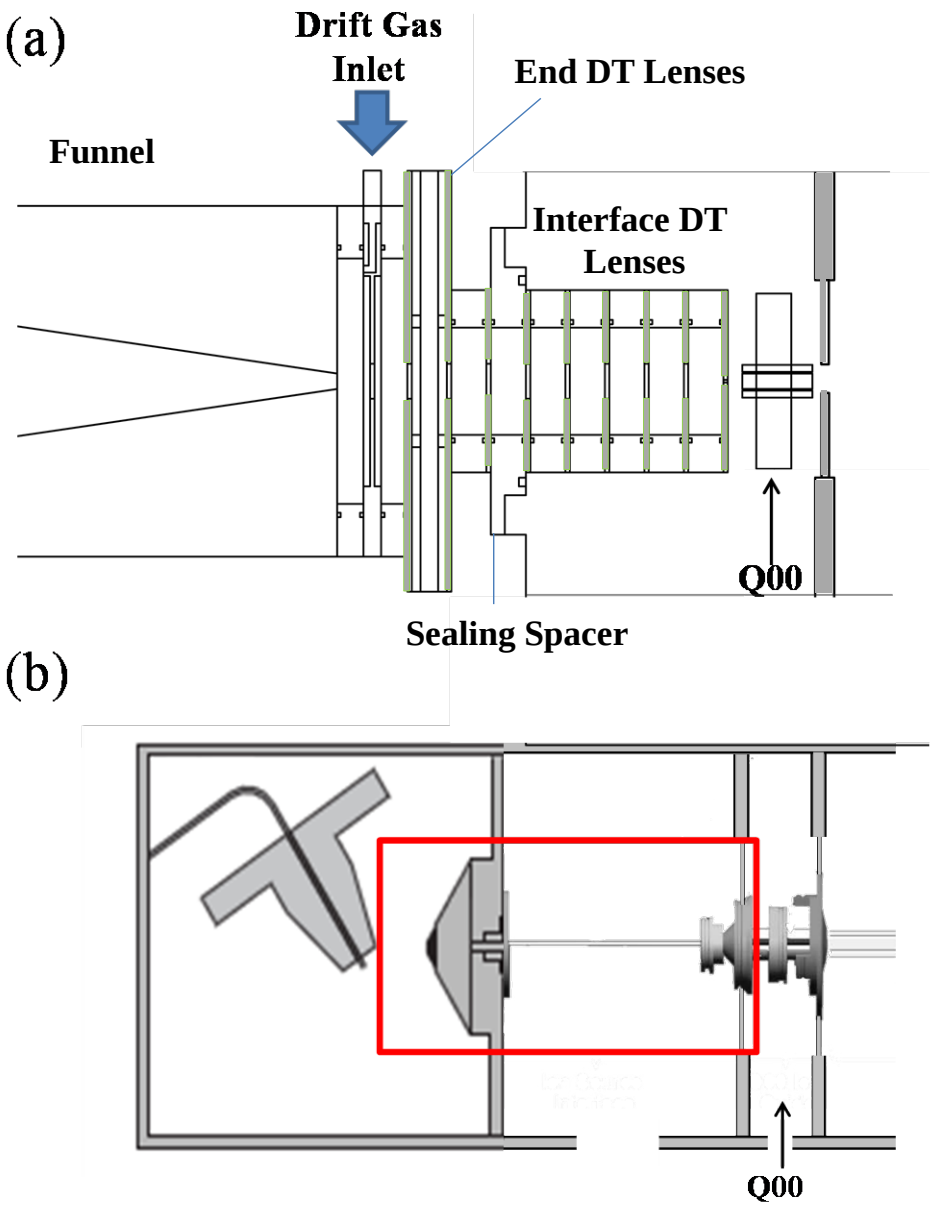

Figure 9. (a) schematic showing the interface designed to couple IMS to the MS entrance. A section of small drift tube lenses takes the place of original sweep cone, transfer tube, tube lens and skimmer (shown in (b) in the red frame) and is inserted into the MS entrance. Seal is made at the entrance of MS. (b) shows the original atmosphere pressure interface of MS.

original interface from atmosphere to vacuum, including the transfer tube, tube lens and skimmer [shown inside the red frame in Figure 9(b)] are removed to accommodate those interface drift lenses. In the original MS, the pressure in the transfer tube and tube lens region is ~1 Torr and

the pressure of the Q00 chamber is ~50 mTorr. When coupling IMS, the pressure of the drift tube matches that of tube lens region and the pressure of Q00 needs to be maintained at the same level as before. This can be accomplished by controlling the aperture size of the last drift tube lens. A lens with 1.00 mm aperture will be used tentatively based on the pressure difference of both sides of the lens: $d = (16P_2S/\pi\Delta P\bar{\upsilon})^{1/2}$, in which d is the diameter of the aperture, P_2 is the pressure of Q00 chamber, S is the pumping speed, ΔP is the pressure difference at two sides of the last lens and $\bar{\upsilon}$ is the average speed of drift gas molecules (in our this case will be ~1.6 km/s for He).

One of the Delrin spacers that insulates these small drift tube lenses is modified to fit and seal the MS entrance [in Figure 9(a)]. Interface drift lenses will be compressed with eight nylon nuts and screws. The shape of lenses and spacers has been revised as shown below in Figure 10. Aperture size are 0.500" for interface drift lenses except the last one. Tabs on the edge of lenses will be used for connecting a circuit board with resistors.

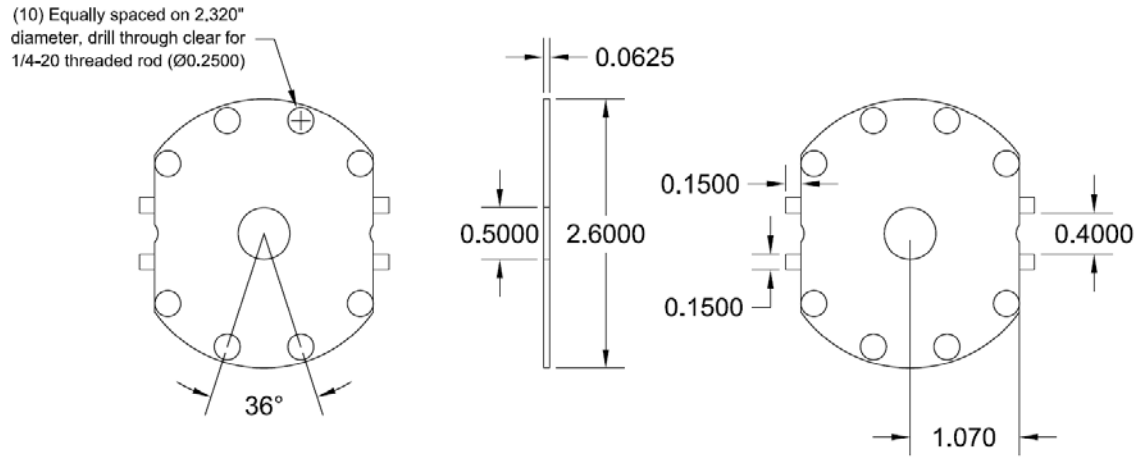

Figure 10. The drawing of interface lenses. Tabs on the side are made for electric connection.

A SIMION (an ion optics simulation program that can calculate electric fields) simulation of the field at the interface region has been carried out. A 14 V/cm DC field was used for the simulation. The

result is shown in Figure 11. The DC field in the ion path is nearly homogeneous, and no strong field that can cause fragmentation of ions is observed.

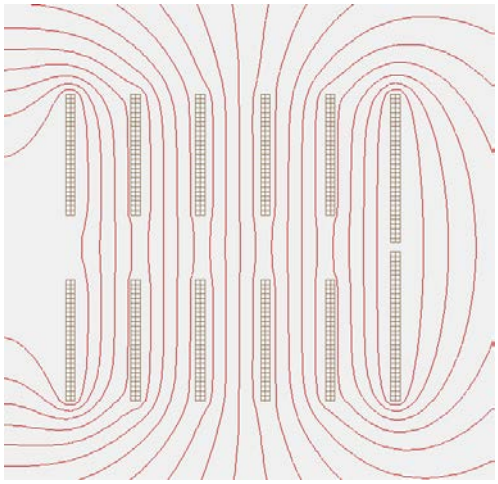

Figure 11. A SIMION (version 8.0) simulation of the electrical field at interface region. The field in the interface path is nearly homogeneous.

2.3.7 Vacuum System

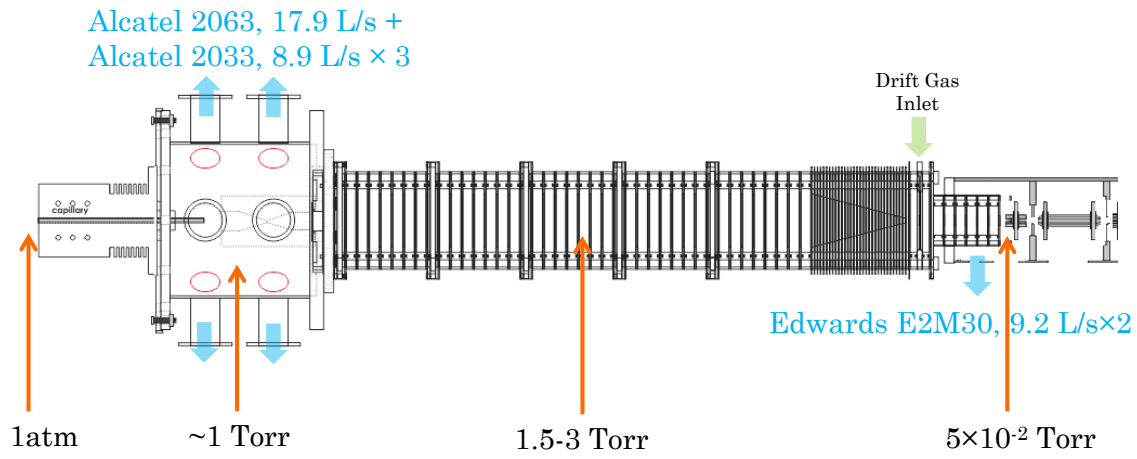

Figure 12. Schematic of the vacuum system of IMS and IM-MS interface.

General information of the vacuum system for the constructed drift tube is shown in Figure 12. The ESI source is atmospheric. The chamber is pumped with speeds of ~45 L/s (Alcatel 2063

and Alcatel 2033, Pfeiffer Vacuum GmbH, France) through six 1.5” I.D., 4 feet reinforced PVC tubings (McMaster Carr, US) and maintained at ~1 Torr. The drift tube and back funnel will be filled with 1.5-3 Torr drift gas leaking in from the end of the back funnel. The leak rate will be controlled by a leak valve going in between the cylinder and the drift gas inlet. The chamber pressure needs to be held slightly lower than the drift tube in order to keep the drift gas going from the drift gas inlet towards the chamber. The forepumps of the MS handle pumping of the IM-MS interface region.

The pressure in the drift tube is monitored by a Baratron (690A Baratron Heated, MKS Instruments, MA, US) connected to the end of the back funnel. The pressure of MS can also be monitored from the LTQ Tune controlling software (Thermo Electron, San Jose, CA, USA).

2.3.8 Electronic System

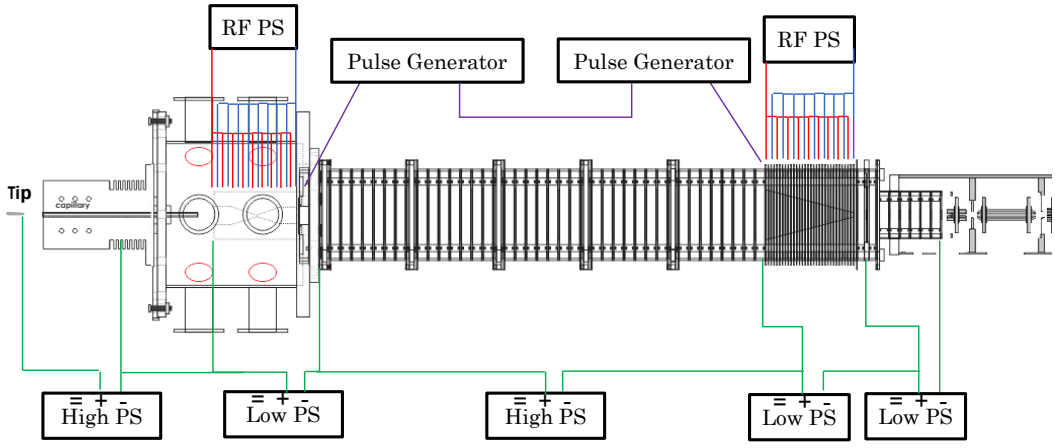

Figure 13. Simplified electronic system of IMS and IM-MS interface. Electronics used are labeled in Figure. Power supplies are floated on those at right side.

In order to guide positively charged ions through the drift tube towards the MS, the strength of the DC field decreases along the drift tube. The potential of each section of the IMS is floated on

the potential of the section on its right by connecting the negative terminal of one power supply to the positive terminal of another which it will be floated on, as shown in Figure 13. In this manner the DC field will be a continuous electrical gradient along the DTIMS. Green lines stand for the connection to DC power supplies. Agilent power supplies with 0-120 V changeable DC output are used to precisely control the potential applied to the funnels. A high voltage power supply will be used to add ~1000 V voltage to the drift tube. The whole source chamber including the source block is floated above the potential of HGF. Another high voltage power supply will be involved to hold the potential of the nanospray tip (Polymicro Technologies, Phoenix, AZ) at 2 kV to 4 kV. Isolation transformers will be used to realize the floating of high potentials. The power supplies that are floated at high potential are grounded to the isolation transformer instead of a normal ground.

For both funnels, RF generators are used to stack RF potentials on the DC potentials. The RF generators have adjustable V_{p-p} and oscillation frequency ranging from 0 - 250 V and 100 – 1000 kHz respectively. Conditions will be optimized according to different type of samples by trial and error. Pulse generators that can output square pulses are connected with the gate lenses. The trigger out of generator for G1 is connected to the trigger in port on pulse generator G2 so that a certain time delay can be set.

Since the factory ion source needs to be removed from the MS when the IMS is coupled with the MS, a jumper is needed to communicate to the software that the source is on. By having a jumper between pins 9 and 10 at the connection above the source will serve this purpose.

2.3.9 Completed Work

Currently, the drift tube and back funnel have been assembled and leak tested. The source chamber including ESI source block with revised design has been machined and received from the machine shop. The assembling of HGF is finished. The printed boards used for HGF have been manufactured by the electronic shop and placed onto the funnel. Electronic tests have been carried out to make sure the connection functions well without leakage. The whole IMS, except the IM-MS interface is connected and ready to be coupled to the LTQ MS when interface parts are completed by machine shop. Partial electronics have been collected and tested. Mechanical pumps are ready to be connected to the source chamber. The photo of the assembled drift tube with the IMS-MS interface is show in Figure 14.

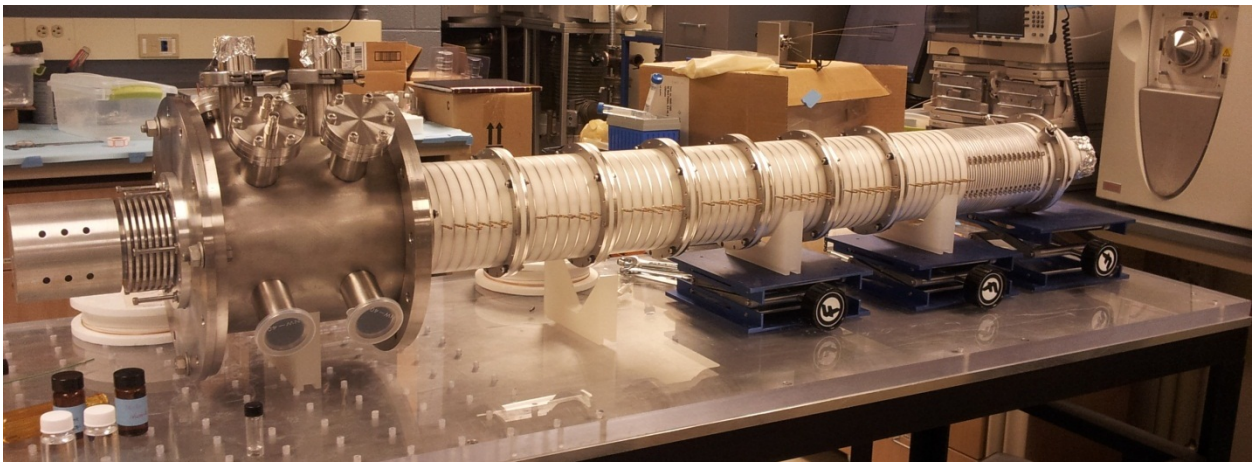

Figure 14. An photo of the assembled drift tube.

Portions of this chapter are based on the following paper:

Hao Bai, Wentao Jiang, Gregg P. Kotchey, Wissam A. Saidi, Benjamin J. Bythell, Jacqueline M. Jarvis, Alan G. Marshall, Renã A. S. Robinson, and Alexander Star. Insight into the Mechanism of Graphene Oxide Degradation via the Photo-Fenton Reaction. J. Phys. Chem. C 2014, DOI: 10.1021/jp503413s

3.0 ANALYSIS OF CARBON NANOMATERIAL DEGRADATION PRODUCTS USING MASS SPECTROMETRY

3.1 BACKGROUND

The degradation of carbon nanomaterial is of great importance. It has been reported that specific enzymes can catalyze the degradation of functionalized CNTs with the presence of H_2O_2. The effectiveness of horseradish peroxidase[59] and myeloperoxidase (MPO)[60] in the degradation process has been demonstrated by Alexander Star and coworkers at the University of Pittsburgh. The final product of degradation is CO_2[59]. Potential degradation intermediates have been proposed to be molecules containing aromatic rings and carboxylic acid groups, for example, mellitic acid.

The enzyme catalyzed degradation of graphene has been reported[61]. Furthermore, recently the degradation of graphene oxide in the photo Fenton system has also been reported[62]. H_2O_2 was used as the oxidative reagent and low concentration Fe^{2+}/Fe^{3+} as the catalyst. The reaction was carried out under UV radiation.

The objective of this project was to elucidate the mechanisms of carbon nanomaterial degradation by MS analysis of the intermediate products generated during the degradation. The

MS-based workflow that has been developed is shown in Figure 15. Briefly, carbon nanomaterials are degraded by H_2O_2 under different conditions. The final product is CO_2. The reaction was stopped before carbon nanomaterial was fully degraded. Intermediates were extracted from the solution and MS and MS/MS were obtained to determine the structure of them. For MPO system in which salt was involved, different extraction methods were developed in order to separate the intermediates from salt. Methods used include Methyl Ethyl Ketone extraction, C18 Ziptip removal of salt, and membrane dialysis. The structural information was further used to elucidate the degradation mechanism. Samples at different reaction points were analyzed to understand the process. In addition to degradation product samples, standards were run to provide basic information of the fragmentation pathway of different functional groups and PAHs. Standards tested generally include aromatic acids and pyrene-based compounds.

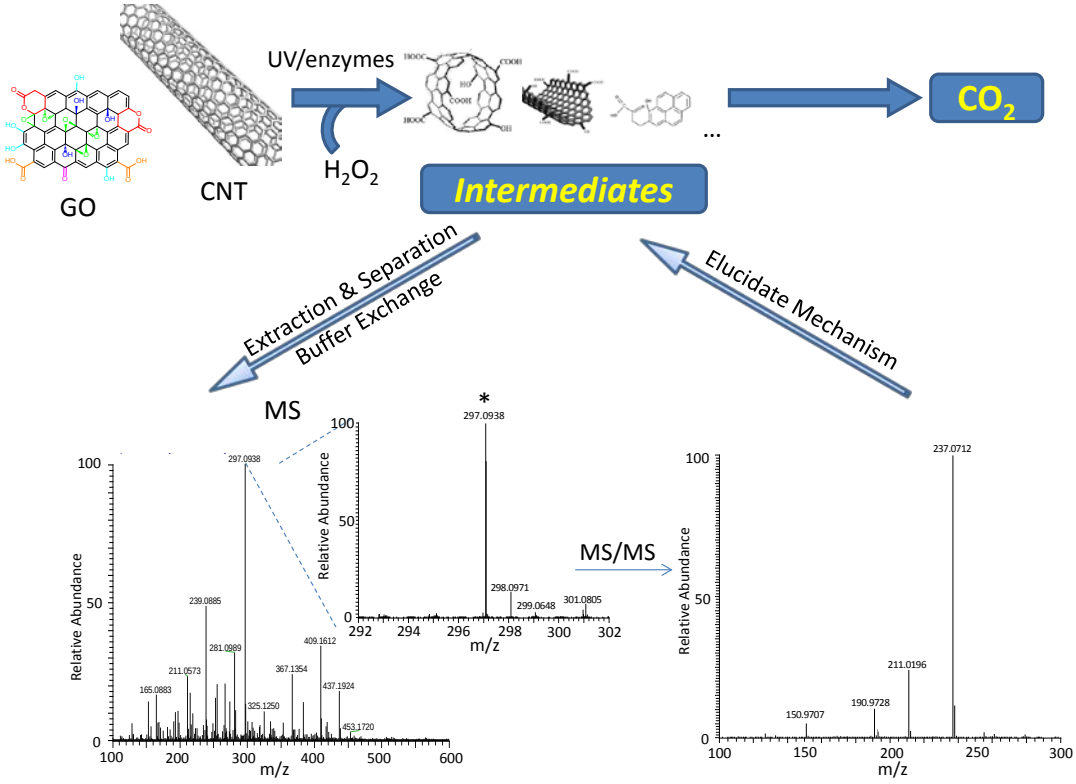

Figure 15. Workflow of carbon nanomaterial degradation intermediates study.

3.2 EXPERIMENTAL

3.2.1 Mass Spectrometry of Potential Standards

Reagents and Materials. Purchased reagents were used as standards. Mellitic acid (benzene-1,2,3,4,5,6-hexacarboxylic acid), trimesic acid (benzene-1,3,5-tricarboxylic acid), benzoic acid, benzaldehyde and phenyl acetic acid are purchased from Sigma-Aldrich. Methanol, water and acetonitrile used are MS grade and purchased from Fisher Scientific.

In addition, three pyrene-based compounds are considered as "smaller graphene systems" and tested by MS in order to gain better idea how the oxidized carbon materials respond to MS analysis. These compounds include pyrene, 1-pyreneacetic acid and 1-pyrenebutyric acid [Sigma-Aldrich Corp. (St. Louis, MO)]. It should be noted that due to the low solubility of these pyrene-based compound, the solid materials were not fully dissolved in the MS solvent. The upper clear solutions were used to obtain MS and MS/MS.

MS conditions. An LTQ Orbitrap-Velos MS instrument (Thermo Fisher Scientific) was employed for mass spectra acquisition. 1 mg/ml standard solutions were prepared by dissolving standards in 50:50 (v:v) H_2O:MeOH or 50:50 (v:v) H_2O:ACN with 0.1% formic acid (FA). Direct infusion experiments were carried out with a nano ESI source. Data were collected in positive mode. The voltage of the nano ESI tip was held at 1.75 kV and the entrance capillary was maintained at 200 ºC. Peaks in parent scan were selected and fragmented using collision induced dissociation to obtain MS/MS spectra.

3.2.2 P3-SWNT Degradation

Reagents and Materials. P3-SWNTs used were purchased from Carbon Solutions, Inc. prepared by arc-discharge process followed by nitric acid treatment in order to get high functionality[63]. This type of SWNTs contains 1.0 – 3.0 atomic percent carboxylic acid. Myeloperoxidase (MPO), Human Neutrophil, was purchased from Athens Research & Technology. NaClO, $FeCl_3$ (hexa-hydrate), 30% H_2O_2 were purchased from Sigma Aldrich. Amplex Red was purchased from Molecular Probes, Invitrogen. Solvents, including H_2O, MeOH, MEK, ACN, Ethyl Acetate, dichloroform and etc. were HPLC grade or Higher.

Incubation of P3-SWNTs with MPO and H_2O_2. 100 µg MPO was suspended in 360 µL pH 7.4 PBS buffer. In a typical experiment, 4 µL of MPO prepared as described above, producing a minimal activity of 800 µU/µL, 15µL of 1mg/mL SWNTs, 1 µL of 18.75mM H_2O_2, 7 µL of 5M NaCl and 180 µL PBS buffer were mixed thoroughly to start the reaction in the incubator at 37 ºC, followed by hourly addition of 1 µL of 18.75mM H_2O_2 eight times per day and daily addition of 4 µL of MPO stock solution. This set of reaction can be scaled up if necessary. This was continued for 4 days. All the stock solutions should be kept in the refrigerator at 4 ºC. Activity of MPO should be tested and verified with Amplex Red before the reaction.

Treatment for Mass Spectrometry. Samples after the reaction were filtered with 0.2 µm Cellulose Acetate Membrane filter paper (Sterlitech Corporation, Kent, WA). Left over SWNTs were collected on the filter paper after overnight drying in the oven. Filtrates were acidified with HCl and collected for further deionization treatment. Different extractions with organic solvent, Ziptip and dialysis were performed. After the purification, solvent was removed by rotary evaporation or Speedy Vac. Sample solution (1 mg/ml) was prepared by resuspending the leftover ma-

terial into ACN:H_2O 50:50 (v:v) with FA or MeOH: H_2O 50:50 (v:v), vortexing gently, and filtering with 0.2 μm filter paper.

Extraction Methods.

1. Extraction with methyl ethyl ketone (MEK) was conducted. Typically, equal volumes of organic solvent and aqueous solution were mixed and shaken vigorously. Extraction was usually performed three times and the organic phase was collected for rotary evaporation.

2. C18 Ziptip (Supelco, Bellefonte, PA) was also used to remove the salt from the sample. First, the Ziptip was solvated with 10 μL ACN (with 0.1% FA) and equilibrated with H_2O (0.1% FA). Sample was aspirated into the Ziptip and dispensed for 3-5 times to allow product binding to the extraction material. Bound species were washed twice with H_2O (0.1% FA) and eluted with ACN (0.1% FA) into an Eppendorf tube.

3. Dialysis was performed utilizing membrane with molecular weight cutoff of 500 Da (Sigma). The reaction products were dialyzed in nanopure water for 2 days to remove the small molecules, ideally, only salts and H_2O_2. Small molecular weight cutoff tubes were applied to reduce the loss of oxidation products. The dialysis time was controlled to balance the desalination and loss of oxidation products.

MS conditions. Both LTQ MS and LTQ Orbitrap-Velos MS instruments (Thermo Fisher Scientific) have been used for mass spectra acquisition. 1 mg/ml degradation product samples in H_2O:MeOH 50:50 (v:v) were prepared, continuously injected from a syringe pump and directly infused into MS with an ESI source. The following electrospray ionization parameters: spray

voltage 4.5 kV, capillary 275 ºC, flow rate 3 µL/min, and a sheath N_2 flow were used. Data was collected with positive mode. Peaks in the parent scan were selected (using an isolation width of 2 m/z) and fragmented to obtain MS2 spectra.

3.2.3 Graphene Oxide (GO) Degradation

Reagents and Materials. All the reagents were used as received without further purification. Graphene Oxide (GO) (5 mg/mL) was purchased from Graphene Supermarket in aqueous Solution. $FeCl_3$ (hexahydrate), 30% H_2O_2 and concentrated HCl were purchased from Sigma Aldrich.

Photo-Fenton Reaction of GO. The photo-Fenton reaction was carried out under vigorous stirring in a 50 mL quartz tube, which is held around 6 cm from the UV lamp (Blak-Ray B100AP, 100-watt longwave UV, supplies fluorescence with ballasted bulb). In a typical experiment, 500 µL of 5 mg/mL GO aqueous solution, 4.5 µL of 30% H_2O_2, 100 µL of 1 mM $FeCl_3$ and 24.6 nL nanopure H_2O were mixed in the quartz tube. The pH of the mixture was adjusted to pH 4 with diluted HCl. The tube was sealed and no further addition of H_2O_2 is added to get a complete degradation of GO in about 3 days. After the reaction, sample after the reaction was filtrated with 0.2 µm filter paper. Left-over GO was collected and the mass was measured on the filter paper after overnight drying in the oven.

MS conditions:

(1) LDI Mass Spectrometry. A Voyager-DE PRO MALDI TOF mass spectrometer (AB Sciex, Framingham, MA, USA) was utilized for LDI data. Filtered/lyophilized day 0, 1, and 3 samples were resuspended in nanopure water at a concentration of 0.2 mg/mL and tested without any matrix. To this end, 10 µL of sample solution was dropped onto a MALDI plate and dried under

ambient conditions. For data acquisition, the instrument settings were: positive reflector mode; 25,000 V accelerating voltage, grid voltage equals 75% accelerating voltage, 1.12 mirror to accelerating voltage ratio, 200 ns; extraction delay, and 2,500 laser intensity with N_2 laser source.

(2) ESI Orbitrap Mass Spectrometry. An LTQ Orbitrap-Velos mass spectrometer (Thermo Fisher Scientific) was employed for mass spectra acquisition. Filtered/lyophilized day 0, 1, and 3 samples (1 mg/mL) were resuspended in 50:50 (v:v) H_2O:MeOH or 50:50 (v:v) H_2O:ACN with 0.1% formic acid (FA) and directly infused into the ESI source at a flow rate of 3 µL/min. Data were collected in positive ion mode. The voltage of the ESI tip was held at 4.5 kV, sheath gas was employed, and the entrance capillary was maintained at 275 °C. Precursor ion mass spectra were obtained in the Orbitrap at 60000 nominal resolving power at m/z 400, and selected ions were fragmented in the dual-pressure LTQ with collision-induced dissociation at normalized collision energy 35% and injection time 25 ms. MS/MS data were recorded in the Orbitrap at 60000 nominal resolving power at m/z 400 unless otherwise noted.

(3) ESI-FTICR. Conditions can be accessed in the full paper: Insight into the Mechanism of Graphene Oxide Degradation via the Photo-Fenton Reaction. J. Phys. Chem. C 2014, DOI: 10.1021/jp503413s.

3.3 RESULTS AND DISCUSSION

3.3.1 Standard MS Analysis

The degradation of CNTs is a process involving the cleavage of C-C bonds and addition of O atoms to carbon atoms [59]. Aromatic rings with carboxylic acids are proposed as the potential deg-

radation products. Mass spectra of several typical aromatic carboxylic acids have been recorded. The parent ion mass spectrum of mellitic acid (1,2,3,4,5,6-hexacarboxylic acid) is shown in Figure 16. A series of peaks losing H_2O molecules from the molecular peak are shown in the spectrum, indicating that the molecular ion of mellitic acid is prone to losing water molecules. The loss of H_2O could result from the dehydration of two adjacent carboxylic groups. The stepwise dehydration structures are shown below the mass spectrum in Figure 16. Parent ion scans were further studied by MS/MS in order to acquire more structural information.

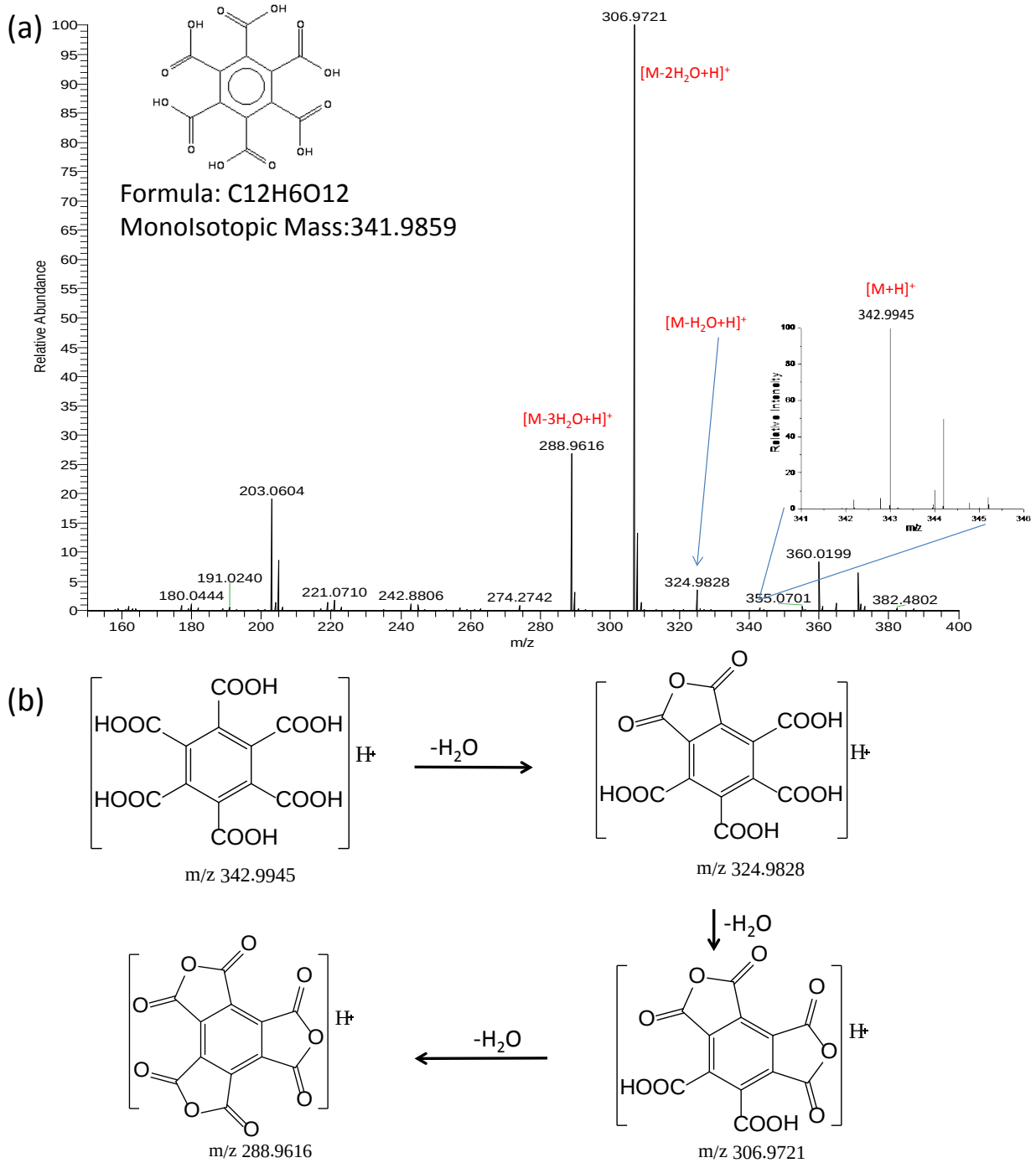

Figure 16. (a) Parent Ion MS of mellitic acid and (b) proposed structures of labeled peaks.

The peak at m/z 288.96 was isolated and fragmented to get the MS/MS spectrum shown in Figure 17. Fragments losing CO_2 and CO molecules were observed. The confirmation of ion formulas is attributed to the high resolution and mass accuracy of Orbitrap mass analyzer. It

should be noted that some ions can adduct a H_2O molecule. Several cases can be seen from the MS/MS spectrum such as $[M\text{-}CO_2\text{+}H_2O\text{+}H]^+$, $[M\text{-}CO_2\text{-}CO\text{+}H_2O\text{+}H]^+$, $[M\text{-}2CO_2\text{-}CO\text{+}H_2O\text{+}H]^+$, $[M\text{-}3CO_2\text{-}CO\text{+}H_2O\text{+}H]^+$ and $[M\text{-}3CO_2\text{-}2CO\text{+}H_2O\text{+}H]^+$.

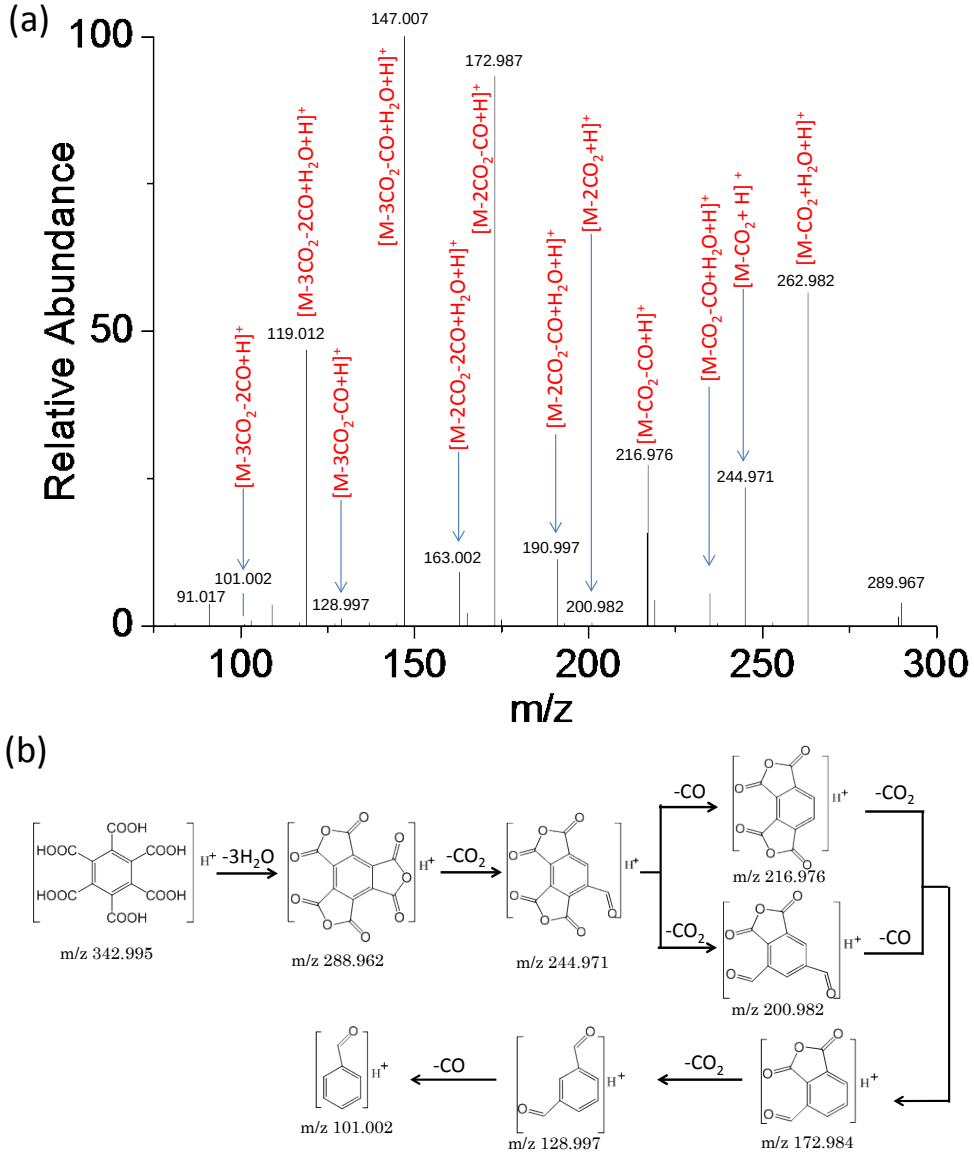

Figure 17. (a) MS/MS spectrum of peak 288.96 selected from parent scan and (b) fragment structures and fragmentation pathway.

Another benzene based carboxylic acid, trimesic acid, was also analyzed by MS. The spectra are shown in Figure 18. From the spectrum on the left, the stepwise H_2O loss (two H_2O molecules were lost in total) was observed. This phenomenon indicates the interesting fact that even when two carboxylic groups are on the meta-position, the dehydration can still occur. Furthermore, peaks with deduction of CO_2 followed by CO (some with H_2O added) are seen in the MS/MS spectrum. The MS spectra of those two standards support and complement each other.

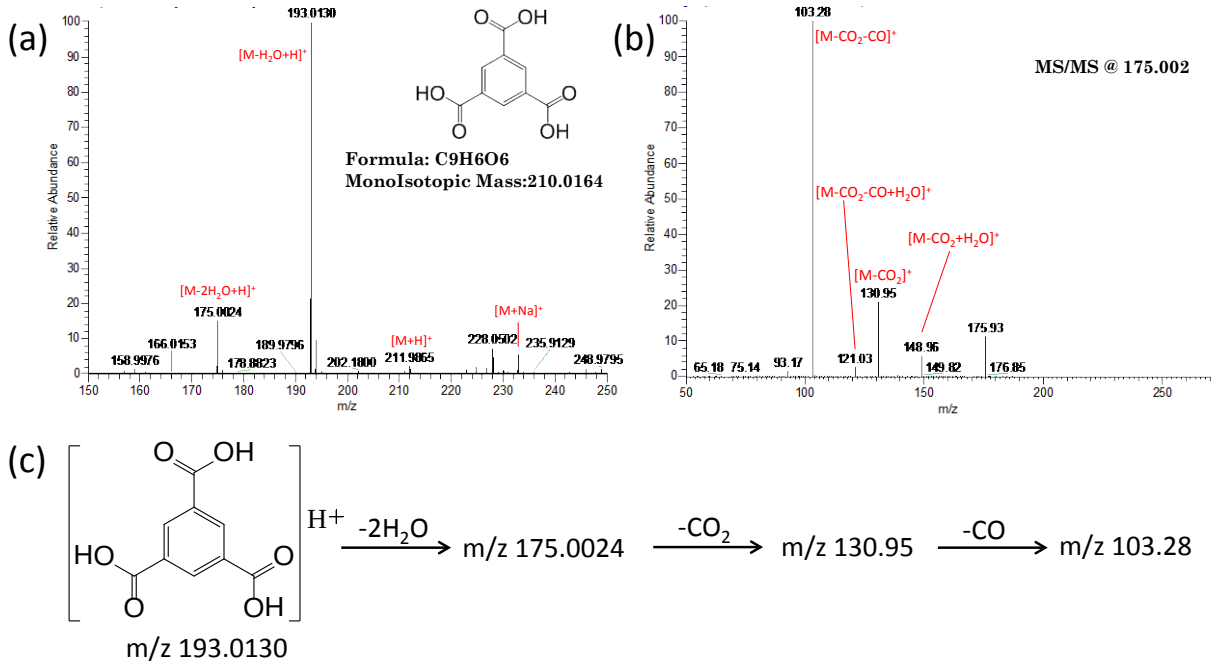

Figure 18. Parent MS and tandem MS of trimeric acid.

Other standards were analyzed by MS to obtain insights to basic fragmentation mechanisms of different functional groups present on benzene. Those standards include benzoic acid, phenylacetic acid, benzaldehyde, and 2,4-dihydroxybenzoic acid. MS/MS spectra are given below in Figure 19. For benzoic acid, loss of both H_2O and CO_2 has been observed, but after the loss of H_2O, no evidence of CO loss was observed. Phenylacetic acid shows sequential deduction

of H_2O and CO, which forms a stable conjugated benzyl cation. In the MS/MS spectrum of benzaldehyde, the fragment losing CO is the only intense peak.

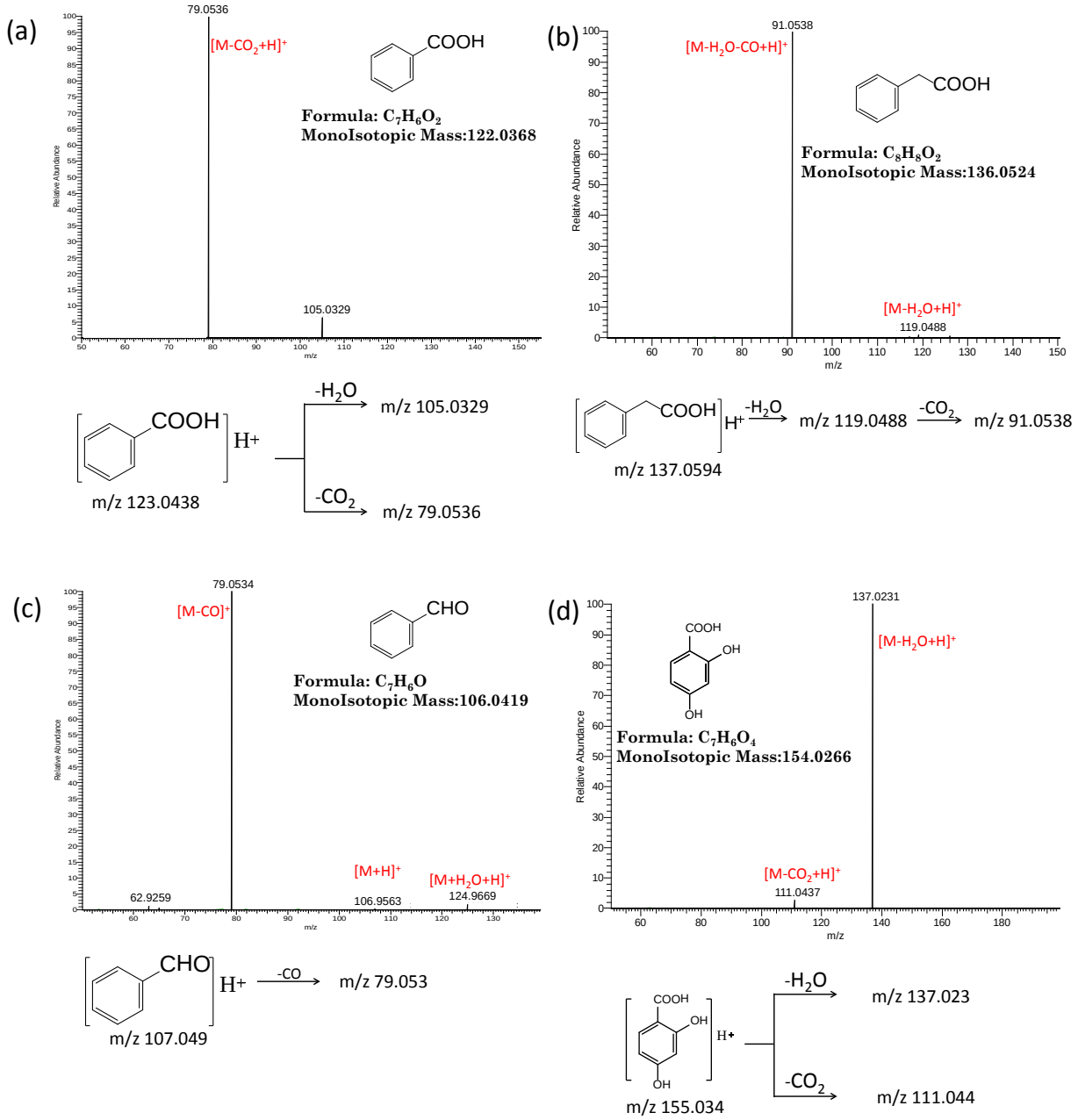

Figure 19. Tandem MS spectra of standards including (a) benzoic acid, (b) phenylacetic acid, (c) benzaldehyde and (d) 2,4-dihydroxybenzoic acid.

The 2,4-dihydroxybenzoic acid ion also has two peaks showing water loss and CO_2 respectively. Compared to benzoic acid, the intensities of those two peaks are reversed, which may

indicate that the addition of an –OH group increases the competing strength of H_2O loss relative to CO_2 loss. Overall, the MS studies of the standard compounds provide a basis for structure determination of degradation products.

Other than these basic standards, others have studied the ESI MS and MS/MS of larger carbon based aromatic molecules[64-67]. For example, in the MS studies of flavone and flavonoid, different mass losses have been observed including CO, C_2H_2O, $C_2H_2O_2$, $C_2H_2O_3$ and so on. Several mass losses have contributed to radicals such as CHO• and •OH. Fragmentation mechanisms were proposed in these papers, which can help to elucidate the mass loss in MS spectra and the structures of degradation intermediates.

CNTs and graphene are both large conjugated carbon systems composed of numerous aromatic rings. Since oxidized CNT and GO can be viewed as the extension of polycyclic aromatic hydrocarbons (PAHs), it can be helpful to study the behaviors of derivatives of PAHs. MS of pyrene and its derivatives have been taken. It is observed that for pyrene, the $[M+H]^+$ is shown at m/z 203.08 in the parent spectra , while the base peak is at m/z 204.08 (Figure 20(a)). It may be caused by the fact that only upper clear solution is used as the MS sample, which can lead to the enrichment of impurities due to the low solubility of pyrene. In the MS/MS, except the selected $[M+H]^+$ peak, ions also exist with a H_2O adduction at m/z 221.08 (Figure 20(c)). In the parent MS of 1-pyreneacetic acid, we see the base peak at m/z 215.20, which corresponds to a loss of CH_2O_2. Also, the MS/MS of the molecular peak gives a strong peak at m/z 215.07. It indicates that the molecule forms a very stable conjugated structure losing CH_2O_2. Different from 1-pyreneacetic acid, 1-pyrenebutyric acid (Figure 20(i)) didn't show a strong trend in losing CH_2O_2. Instead, the loss of H_2O was dramatic in both parent MS and MS/MS. Other peaks in the spectra, which could not be assigned accordingly, may be due to impurities.

Based on the MS results, we can see that for the tested PAHs and derivatives, the structures of PAH are stable during the ESI-MS process, while fragmentations and neutral losses only happen at the side chains or functional groups. It indicates the high stability of PAHs in ESI conditions and serves as evidence for the prediction that if the intermediates of carbon nanomaterial degradation products are derivatives of PAHs, the PAH structures will remain intact in parent MS.

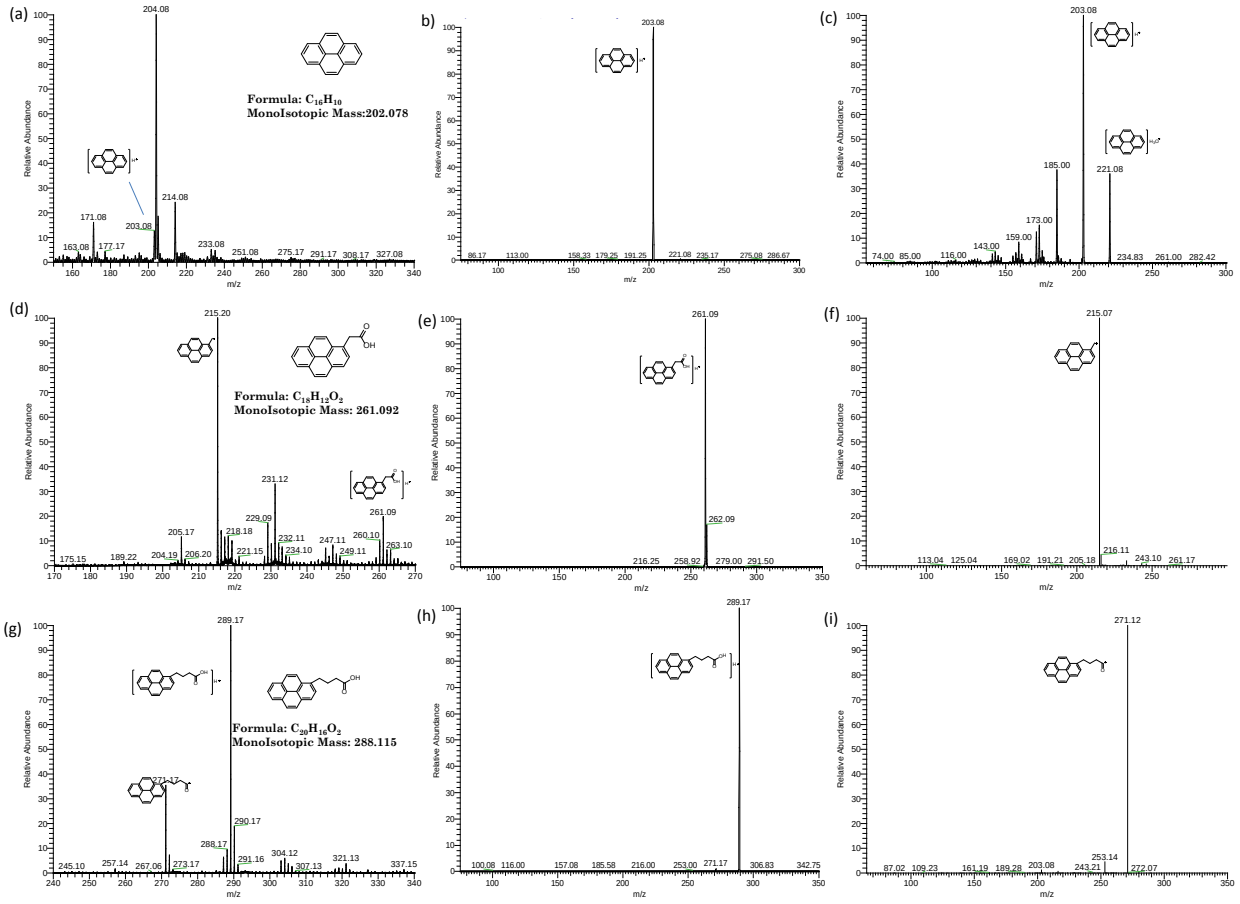

Figure 20. Parent MS and MS/MS of pyrene and its derivatives. (a) (d) (g)parent MS of pyrene, 1-pyreneacetic acid and 1-pyrenebutyric acid respectively; (b) (e) (h) isolation of molecular peak in MS of pyrene, 1-pyreneacetic acid and 1-pyrenebutyric acid respectively; (c) (f) (i) MS/MS of molecular peaks in MS of pyrene, 1-pyreneacetic acid and 1-pyrenebutyric acid respectively.

The neutral losses of standards involved are summarized in table 2 below.

Table 2. Summary of neutral losses of analyzed standards

Neutral Loss (Da)	Elemental Composition	Compounds
18	H_2O	mellitic acid, trimesic acid, 2,4-dihydroxybenzoic acid, 1-pyrenebutyric
28	CO	mellitic acid, trimesic acid, phenylacetic acid, benzaldehyde
44	CO_2	mellitic acid, trimesic acid, benzoic acid, 2,4-dihydroxybenzoic acid
46	CH_2O_2	1-pyreneacetic acid

3.3.2 P3-SWNT MPO Degradation Products Analysis

Figure 21(a) shows the MS spectrum acquired for P3-SWNT degradation products after a reaction time of 120 hours under the catalysis of MPO extracted by MEK. A series of peaks was observed in the spectrum. However, in comparison with the control spectrum (control sample, see Experimental Section 3.2) most peaks shown in the product sample spectrum were also observed in the control sample spectrum (Figure 21(b)). The similarity of the two spectra suggests that those peaks could be impurities from the original reactant materials or introduced during the extraction procedure and do not represent degradation products.

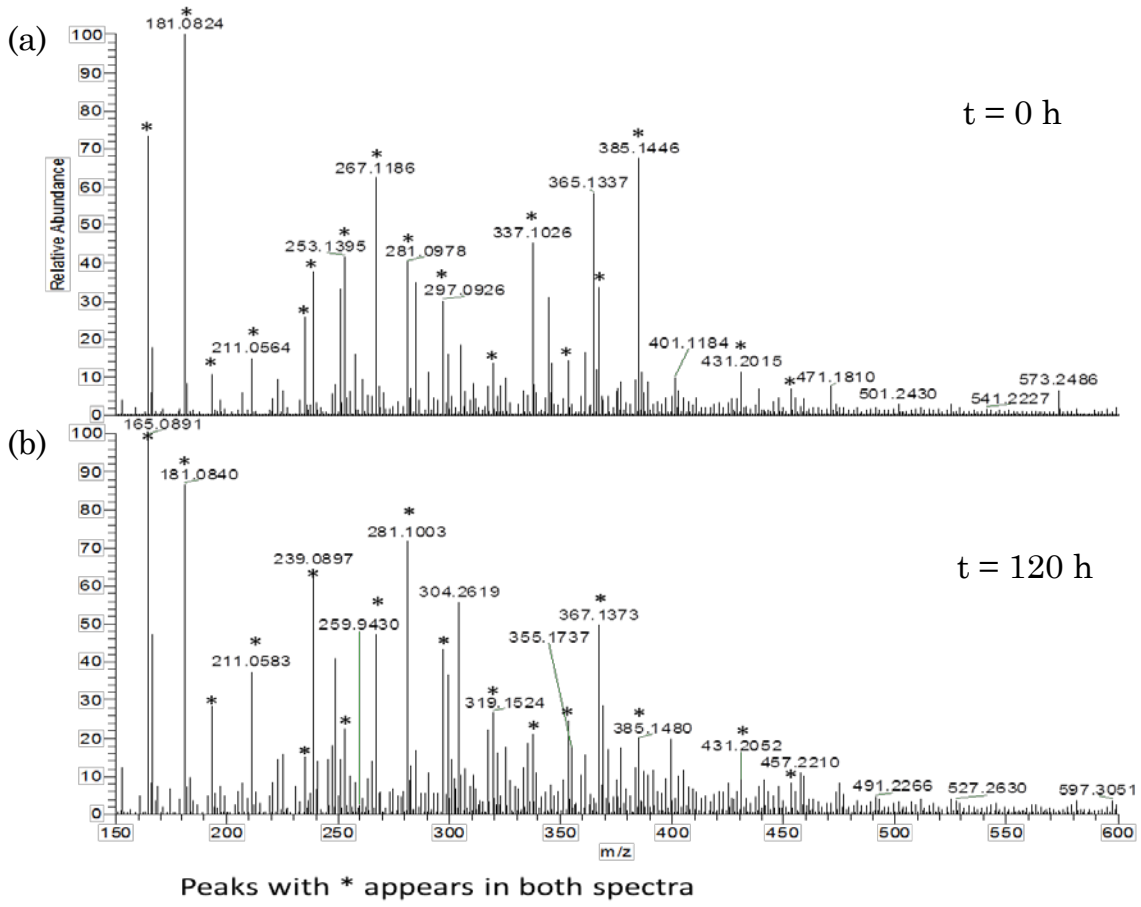

Figure 21. Comparison of spectra of degradation time (a) t = 0 h sample and (b) t = 120 h sample. Intense peaks shared in both spectra are labeled with *.

In order to distinguish degradation products from impurities, different extraction methods were applied including MEK extraction, Ziptip purification and dialysis. The main purpose of performing extraction was to remove NaCl added to the reaction which interferes with ESI of products. MS data for each extraction method were collected. For each extraction method, the spectrum of the control sample and product sample still shared considerable overlap in detected peaks. In addition, MS spectra for the three extraction methods were dramatically different (Figure 22), which means the data of one method can not be supported by others. A collection of MS spectra of product samples for 96 hours reaction using three extraction methods are shown in Figure 22.

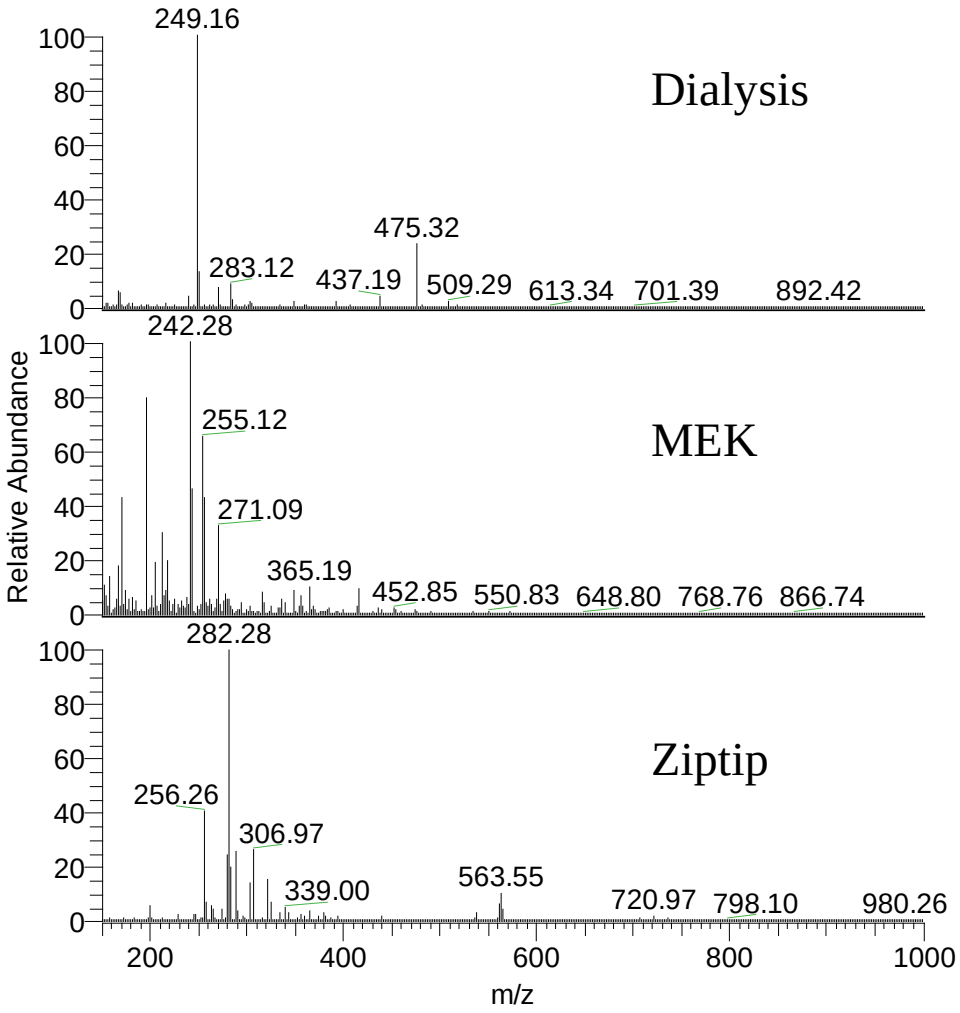

Figure 22. Comparison of MS spectra acquired for product samples extracted from different methods. From top to bottom are spectra of dialysis, MEK, Ziptip extraction respectively.

According to the MS results, MEK extraction still extracts salts, which is not favorable for ESI-MS analysis. Ziptip is a small reversed phase column on which nonpolar substances have better retention while polar and ionic substances are not retained. However, since products are predicted to be carboxylic acids, they may not have good retention on the Ziptip, which means products have the risk of being washed away. Finally, for the dialysis process, the membrane used has a cutoff of molecular weight (MW) of 500 Da, which can lead to the loss of products

whose MWs are less than 500 Da. Those facts indicate that those extraction methods suffer from several shortcomings. Further studies with the SWNT degradation products are still required.

Since GO can be considered as "unzipped" SWNTs[68], the degradation process could be similar. Recently the Photo-Fenton system was demonstrated to be effective on degradating GO[62]. This system does not involve the use of salt and buffer. Thus, we investigated GO degradation in Photo-Fenton system.

3.3.3 GO Degradation Products Analysis

Photo-Fenton reaction which involves ultra-violet radiation catalysis with Fe^{2+}/Fe^{3+} and H_2O_2 was used to degrade GO. Compared with the MPO enzyme catalysis system, the Photo Fenton system do not require buffer to maintain its pH (HCl is used to maintain pH = 4) nor high concentration of NaCl. The only source of salt in this reaction solution is catalytic amounts of Fe^{2+}/Fe^{3+}, which implies that the reaction solution can be directly analyzed by MS without additional steps. It has been characterized by AFM that the mean size of the GO used has a broad distribution of 589 ± 700 nm. After 1 day of incubation under the photo-Fenton conditions, the GO flakes in the dispersion are more narrowly distributed in size, undergo ~40% reduction to 358 ± 186 nm, and demonstrate a thickness increase of ~15% versus day 0, which may be attributed to further oxidation. After the photo-Fenton reaction proceeded for 3 days, small particles with a mean diameter of 36 ± 10 nm and thickness ranging from 2 to 5 nm are present, indicating that graphene quantum dots (GQDs) are successfully formed from the oxidation of GO, and in the bulk dispersion, the GQDs exist as multiple layers due to van der Waals interactions.

As seen in Figure 23A, the GO solution, which is initially dark brown in color, became lighter and virtually colorless with time, this providing empirical evidence of GO oxidation catalyzed by the photo-Fenton reaction. The fluorescence of the starting material (i.e., GO) and products derived from the photo-Fenton reaction after one and three days was examined (Figure 23B). Upon excitation at 325 nm, GO demonstrates a broad peak that is centered on 430 nm. By day 1, the fluorescent intensity increased 154% versus day 0, and its spectrum is both broad and centered on 430 nm. Finally, the fluorescence intensity on day 3 increases 1814% and 1175% versus day 0 and 1, and its sharp peak is centered at ~440 nm. This increase in fluorescence provides evidence that GO is broken down into conjugated products (e.g., oxidized PAHs and/or GQDs).

MS was implemented to elucidate the products of oxidation. Figure 23C depicts the laser desorption ionization (LDI) time-of-flight (TOF) mass spectra corresponding to products obtained at days 0, 1, and 3 after the start of the photo-Fenton reaction. The LDI TOF MS data reveal the presence of carbon clusters ranging from 1000 to 5000 Da (~C100 to C400) in the day 0 and day 1 sample (Figure 23C); these large clusters are not observed in the day 3 sample (Figure 23C). Carbon cluster peaks are spaced by 24 Da across the mass spectra and correspond to the mass of two carbon atoms. It should be noted that because these peaks correspond to carbon clusters smaller in size than the flakes detected by AFM, these clusters may represent fragments generated via laser ablation of larger flakes of GO. By day 3, large GO flakes are broken down into smaller quantum dots (as evidenced by AFM); therefore, the carbon cluster ions do not appear in the MS spectrum.

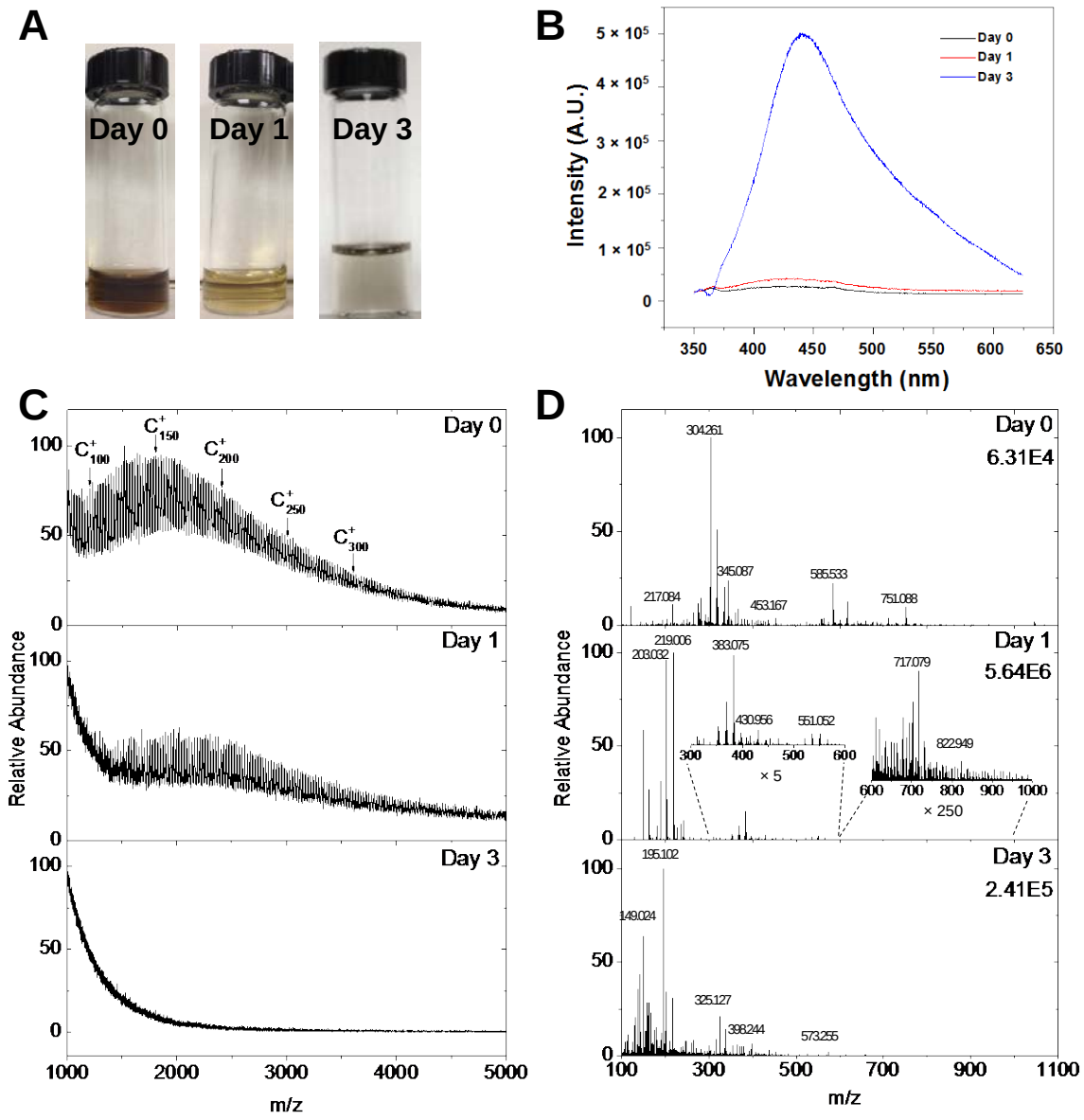

Figure 23. (A) Photograph depicting vials of graphene oxide solution after 0, 1, and 3 days of the photo-Fenton reaction. (B) Fluorescence spectra of the solutions contained in (A) (Apendix 1). (C) LDI-TOF MS and (D) Orbitrap ESI-MS spectra for sample after 0, 1, and 3 days of the photo-Fenton reaction.

Figure 23D displays the electrospray ionization (ESI)-Orbitrap MS spectra of degradation products on days 0, 1, and 3. As observed from the spectra, larger magnitude signal and features are present on day 1 in comparison to days 0 and 3. In particular, numerous peaks are detected from m/z 300-1000 on day 1.

The ESI-Orbitrap MS findings for day 1 degradation products were compared to MS data obtained by 9.4 T ESI Fourier transform ion cyclotron resonance (FT-ICR) mass spectrometry (from National High Magnetic Field Lab, Florida). Figure 24 compares the precursor ion mass spectra obtained. There is considerable overlap between ions observed from both analyses despite variations in the magnitude of signal; which may be partially attributable to inherent differences in the source conditions.

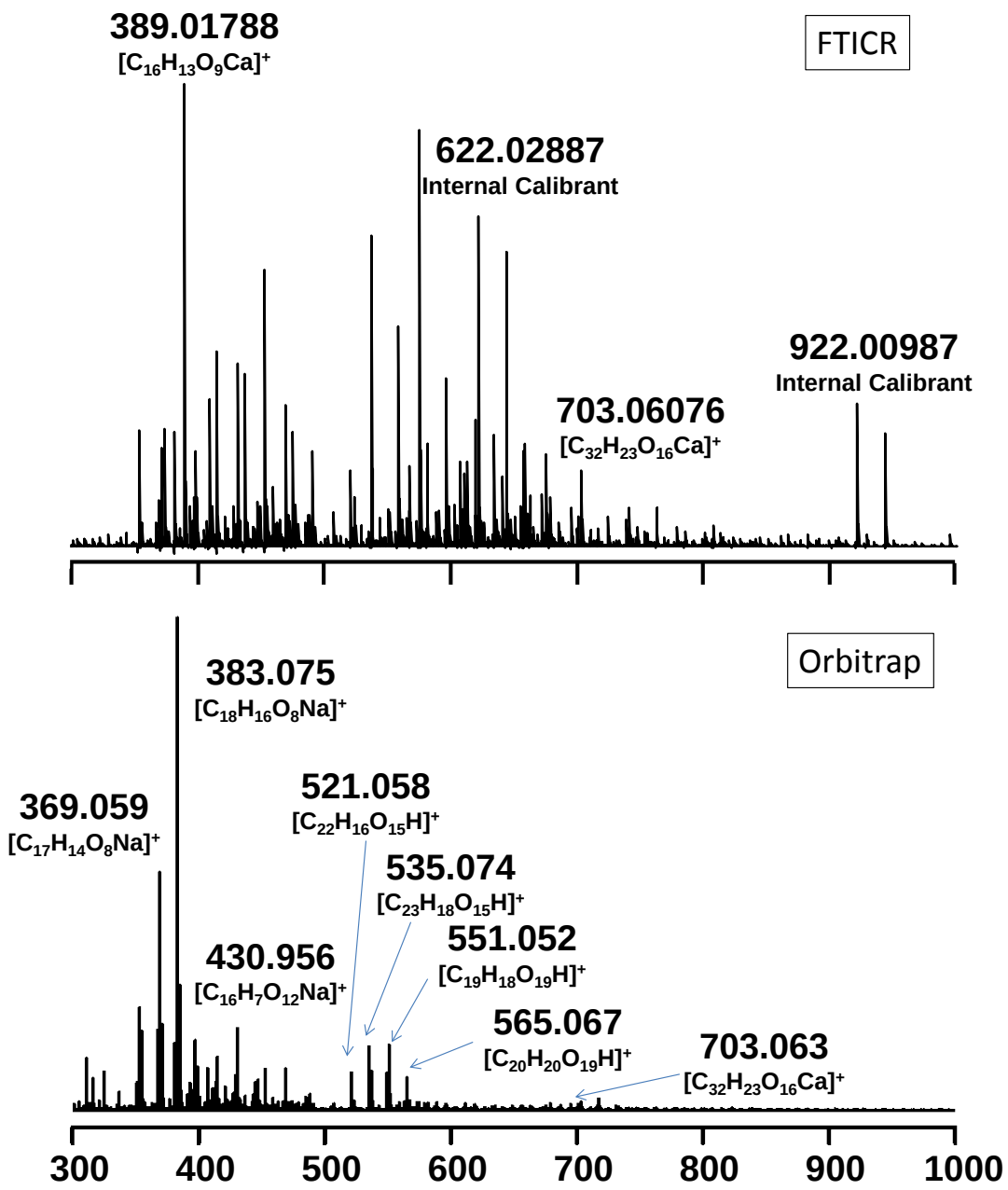

Figure 24. Parent scan spectra derived by ESI-FTICR MS (top) and ESI-Orbitrap MS (bottom) for graphene oxide after 1 day of treatment with the photo-Fenton reaction.

High mass measurement accuracy obtainable with both instruments was used to make assignments of elemental composition. Due to the complexity of the datasets however, only selected species were isolated and exposed to gas-phase fragmentation in order to better deduce chemical composition and possible structures.

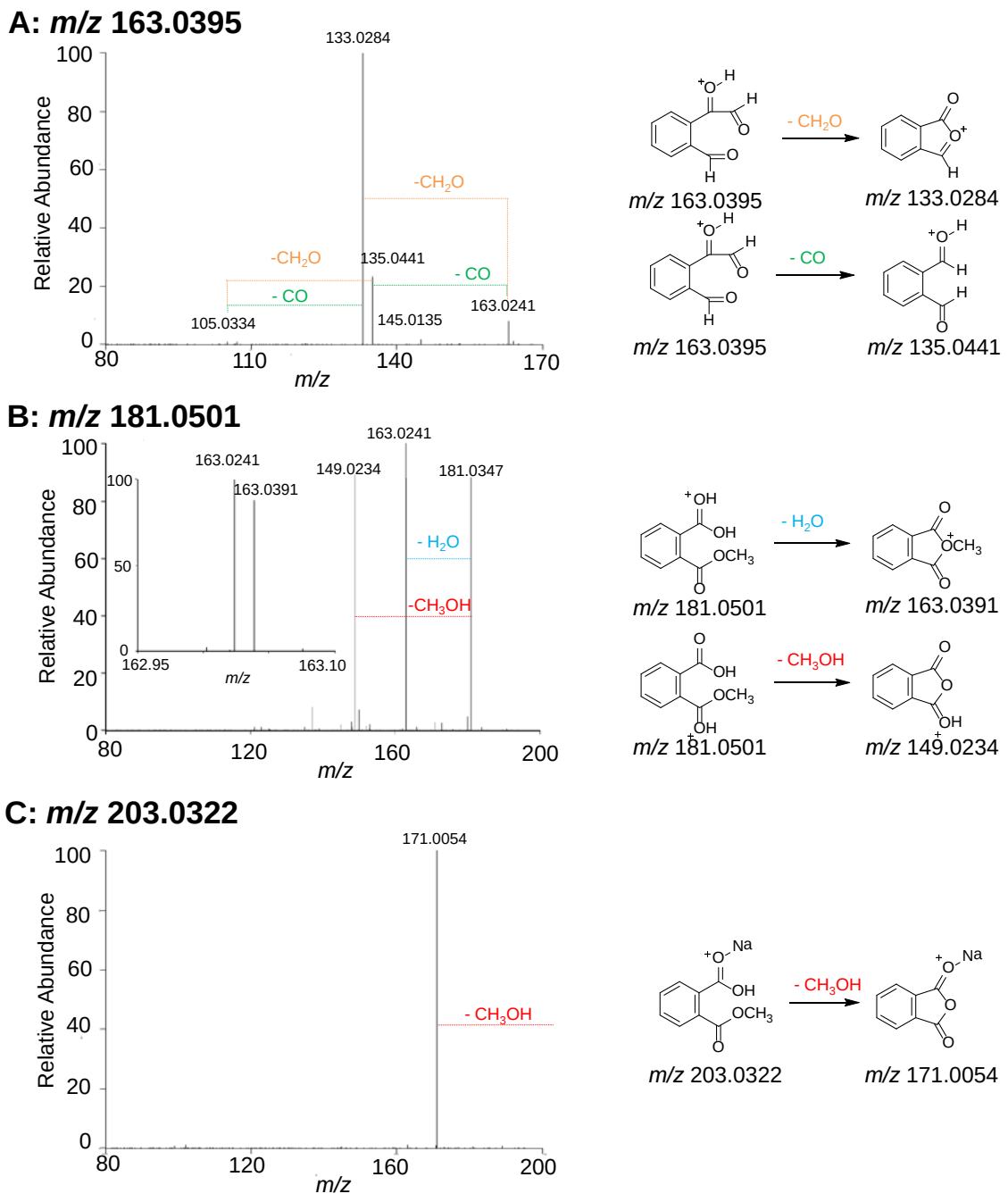

Figure 25. MS/MS spectra of parent precursors from Orbitrap MS analyses of ions with m/z (A) 163.040, (B) 181.050 and (C) 203.032. Structures for (A) – (C) and proposed fragmentation pathways are shown on the right.

For example, peaks at m/z 149.024, 163.040, 189.017, and 203.032, which have the greatest magnitude in the parent scans of the Orbitrap MS data, demonstrate the fragmentation

patterns observed in Figure 25. In the low m/z region of the parent spectrum (Orbitrap MS) a series of peaks related to phthalic acid is observed as follows: the protonated phthalic acid peak (m/z 167.034,$[C_8H_6O_4+H]^+$, -0.56 ppm), a potassiated acid peak (m/z 204.990, $[C_8H_6O_4+K]^+$, -0.81 ppm), protonated phthalic anhydride (m/z 149.024, $[C_8H_4O_3+H]^+$, -0.06 ppm), and the fragment species of protonated phthalic anhydride with the loss of a neutral CO molecule (m/z 121.029, $[C_7H_4O_2+H]^+$, -1.61 ppm). To confirm the assignment of these peaks a standard solution of phthalic acid was also analyzed by ESI-Orbitrap MS and the mass spectrum has similar distributions in the precursor and MS/MS data from the day 1 sample (Figure 26). Building on the phthalic acid peaks, the ion at m/z 181.050 (Figure 25B) has been assigned to monomethylphthalate. The monomethylphthalate ion was observed in the parent spectrum both as a sodiated acid precursor (m/z 203.032, $[C_9H_8O_4+Na]^+$, 1.83 ppm) and as the protonated anhydrous mono-methylphthalate species (m/z 163.040, $[C_9H_6O_3+H]^+$, -0.12 ppm). MS/MS of m/z 181.050 produces fragment peaks corresponding to the loss of methanol and water. The anhydride at m/z 163.040 undergoes two fragmentation pathways (Figure 25A) corresponding to neutral losses of CO or CH_2O. Further confirmation support for these assignments is provided by the MS/MS spectra of the sodiated adduct of mono-methylphthalate (Figure 25C). A single fragment peak corresponding to the loss of the neutral methanol is observed.

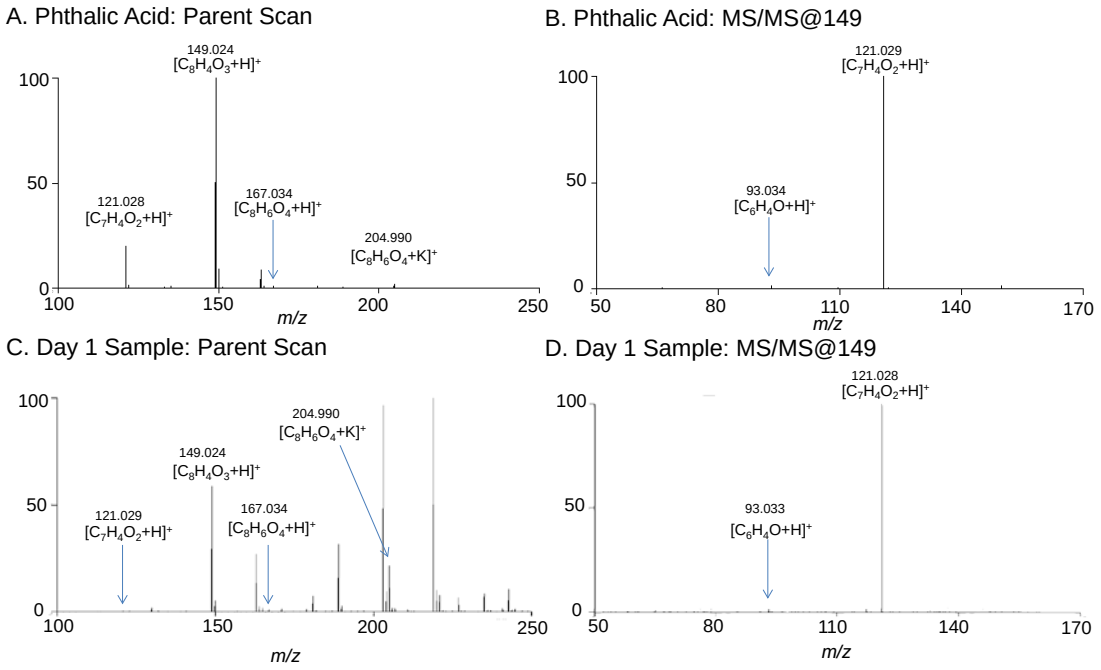

Figure 26. (A) Parent scan spectra of phthalic acid and (B) MS/MS fragmentation pattern of m/z 149 derived by Orbitrap ESI-MS. (C) Parent scan spectra for graphene oxide after 1 day of treatment with the photo-Fenton reaction and (D) MS/MS fragmentation pattern of m/z 149 derived by Orbitrap ESI-MS.

Based on the errors associated with the peaks in the precursor and fragment mass spectra and the associated calculated degrees of unsaturation, aromatic rings, and the presence of C=O bonds are necessary. Structural information is limited to adjacent aromatic rings or anhydride structures. The ion observed at m/z 389.01855 in both datasets was selected for FT-ICR MS/MS. This species was assigned an elemental composition ($[C_{16}H_{13}O_9Ca]^+$, -0.3 ppm error) based upon isotopic verification. After short irradiation periods, sequential neutral losses of m/z 18 yielded a fragment ion at m/z 352.99721 ($[C_{16}H_9O_7Ca]^+$. After longer irradiation, an additional neutral loss of m/z 148 ($C_8H_4O_3$) was seen (also by Orbitrap MS/MS).

Similar FT-ICR MS/MS behavior is seen for precursor ions of m/z 703 ($[C_{32}H_{23}O_{16}Ca]^+$, this time with successive neutral losses of $C_8H_6O_4$. It is worth noting that elemental composi-

tions could be assigned to other neutral losses, even in cases for which the precursor ion composition could not be assigned. Thus, we have high confidence in the assignments for neutral losses.

Overall, the ESI-MS data point to the presence of degradation products that are higher in abundance at day 1 than for days 0 and 3. This observation supports the hypothesis that oxygen sites on GO are oxidized immediately after the initiation of the photo-Fenton reaction, and when combined with the degradation of GO flakes, intermediate species (with MW 150-1000) are generated by day 1. After a period of time between day 1 and 3, these intermediates are no longer heavily present, and the system is dominated by GQDs.

The behavior of mellitic and phthlatic acid with positive mode ESI-MS can be used to make the following assumptions about the day 1 degradation parent MS spectra. 1) The degradation spectra will contain signal from the protonated precursor and peaks associated with loss of neutrals (i.e., H_2O, CO, and CO_2) for carboxylic acids. 2) The degradation spectra may also contain signal from the acid with different cations (i.e, H^+, Na^+, K^+, and Ca^{2+}) which is expected for ESI.[69] These two factors add to the complexity of the parent MS data for degradation products. Furthermore, the co-isolation of precursors that are close in m/z produces MS/MS spectra that are difficult to assign at the resolving power of the Orbitrap.

It is apparent from the MS and MS/MS data, however, that phthalate species exist.[70,71] In addition to the low m/z peaks that correspond to phthalic anhydride and acid, several peaks with higher m/z show losses corresponding to neutral phthalic anhydride or acid molecules (low ppm Orbitrap errors). Such species may arise from homogeneous and heterogeneous clusters of phthalate species with various cations. The presence of a peak at m/z 149.024 is diagnostic for

phthalates detected by various ionization sources in MS.[70-72] This ion is present in the ESI-Orbitrap MS data for degradation samples. Phthalates are common contaminants in plasticizers[73] and arise as background ions in ESI-MS.[74] The presence of these species in GO degradation samples indicates either their formation during degradation of GO flakes or increased extraction of these species from sample vials after the degradation process. Samples were handled in glassware during the degradation and transferred to Eppendorf vials for MS analysis. Thus, the introduction of these species could only arise after the degradation process from the pipette tips, Eppendorf vials, or solvents used for MS analysis if they were not present *a priori* in the sample. The magnitude of signals corresponding to the protonated phthalic anhydride (m/z 149.024) and phthalic acid (m/z 167.040) peaks increases by three and two orders of magnitude from day 0 (control) to day 1 samples. There is a decrease in the relative signal of these peaks of 92% and 43% respectively from day 1 to day 3 samples. Further separation prior to MS will be necessary in order to fully understand all observed degradation products.

3.4 CONCLUSIONS

MS analysis has been carried out for degradation products of carbon nanomaterials. For GO samples degraded by Photo-Fenton reaction, degradation intermediates largely consistes of adja-cent aromatic rings with carboxylic acid groups. Other systems such as SWNT degradation by H_2O_2 in the presence of MPO as catalyst are still being investigated. The GO degradation process may be a former step of enzyme catalyzed SWNT degradation system which demonstrates the necessity of these studies.

Although structures have been proposed for peaks, further confirmation is still needed. The most straight forward method to confirm structures is to find pure chemicals of the proposed product molecules and analyze them by MS and MS/MS. If the spectra of pure chemicals match the spectra of products, it will be a convincible demonstration of the proposed structures. Even if the spectra do not match, the pure chemical can still be taken as a standard to provide more information which can be further used to revise the proposed product structures. Products will be confirmed by this trial and error procedure.

On the other hand, an LC system in the laboratory has been recently coupled to the LTQ MS, so further analysis by LC-MS is possible. Since the degradation samples are complex mixtures (e.g., m/z 163.0386 and 163.0228), a separation before MS detection may significantly help in the removal of interferences and improve detection of products of interest.

4.0 CONCLUSIONS AND FUTURE WORK

A DTIMS-LTQ MS instrument has been designed based on the reported DTIMS setup[43], and partially built. After completion, it can carry out fast separation at scale of μs and further analysis with MS and MS/MS. It benefits the fast analysis of complicated mixture samples by combining the fast speed of IMS and qualitative and quantitative power of MS, and can be used in proteomics, metabolism, degradation products, etc.

For optimization purposes, proteins that are well-studied by IM-MS, such as ubiquitin, bradykinin, can be tested first [75]. Electronics will be adjusted to make sure the system functions efficiently. Transmission efficiency will be evaluated based on the intensity of peaks in MS spectra comparing to the intensity without IMS. Since the exiting aperture of drift tube interface is relative small, the ion loss could be considerable. The interface drift lenses can be revised to a small funnel assembly if the sensitivity is not as good as stand-alone LTQ MS.

The study of carbon nanomaterial degradation products and mechanism is a crucial factor to the efficient application of carbon nanomaterial in biomedical area. Our project proposed a plausible mechanism of the degradation of GO under Photo-Fenton system, and is a very important step towards fully understand the mechanism of the degradation process, which can serve as the basis for the improvement of bio-compatibility of carbon nanomaterial and better and safer use of it.

Different degradation systems will be further studied in order to propose a complete picture of carbon nanomaterial degradation mechanisms. To achieve this objective, a MS and MS/MS library for small molecules including PAHs and their derivatives will be built in order to

facilitates the interpretation of degradation product MS. Furthermore, separation techniques such as LC and IMS will be used before the acquisition of MS in order to get simpler parent MS and more information about species of low concentration, and address the issue of co-isolation in MS/MS.

REFERENCES

(1) Eiceman, G. A. *TrAC, Trends Anal. Chem.* **2002**, *21*, 259.

(2) Marquez-Sillero, I.; Aguilera-Herrador, E.; Cardenas, S.; Valcarcel, M. *TrAC, Trends Anal. Chem.* **2011**, *30*, 677.

(3) Armenta, S.; Alcala, M.; Blanco, M. *Anal. Chim. Acta* **2011**, *703*, 114.

(4) Mäkinen, M.; Nousiainen, M.; Sillanpää, M. *Mass Spectrometry Reviews* **2011**, *30*, 940.

(5) Ewing, R. G.; Atkinson, D. A.; Eiceman, G. A.; Ewing, G. J. *Talanta* **2001**, *54*, 515.

(6) Tam, M.; Hill, H. H. *Analytical Chemistry* **2004**, *76*, 2741.

(7) Kolakowski, B. M.; Mester, Z. *Analyst (Cambridge, U. K.)* **2007**, *132*, 842.

(8) Mäkinen, M. A.; Anttalainen, O. A.; Sillanpää, M. E. T. *Analytical Chemistry* **2010**, *82*, 9594.

(9) Mason, E. A.; McDaniel, E. W. In *Transport Properties of Ions in Gases*; Wiley-VCH Verlag GmbH & Co. KGaA: 2005, p 1.

(10) Nikolaev, E.; Boldin, I.; Jertz, R.; Baykut, G. *Journal of The American Society for Mass Spectrometry* **2011**, *22*, 1125.

(11) O'Donnell, R. M.; Sun, X.; Harrington, P. d. B. *TrAC, Trends Anal. Chem.* **2008**, *27*, 44.

(12) McLean, J. A.; Ruotolo, B. T.; Gillig, K. J.; Russell, D. H. *Int. J. Mass Spectrom.* **2005**, *240*, 301.

(13) Uetrecht, C.; Rose, R. J.; van, D. E.; Lorenzen, K.; Heck, A. J. R. *Chem. Soc. Rev.* **2010**, *39*, 1633.

(14) McDaniel, E. W.; Martin, D. W.; Barnes, W. S. *Review of Scientific Instruments* **1962**, *33*, 2.

(15) Kebarle, P.; Hogg, A. M. *The Journal of Chemical Physics* **1965**, *42*, 668.

(16) Hoaglund, C. S.; Valentine, S. J.; Sporleder, C. R.; Reilly, J. P.; Clemmer, D. E. *Analytical Chemistry* **1998**, *70*, 2236.

(17) McAfee, K. B., Jr.; Sipler, D.; Edelson, D. *Physical Review* **1967**, *160*, 130.

(18) Baker, E. S.; Clowers, B. H.; Li, F.; Tang, K.; Tolmachev, A. V.; Prior, D. C.; Belov, M. E.; Smith, R. D. *Journal of The American Society for Mass Spectrometry* **2007**, *18*, 1176.

(19) Johnsen, R.; Brown, H. L.; Biondi, M. A. *The Journal of Chemical Physics* **1970**, *52*, 5080.

(20) Wu, C.; Siems, W. F.; Asbury, G. R.; Hill, H. H. *Analytical Chemistry* **1998**, *70*, 4929.

(21) Hilton, C. K.; Krueger, C. A.; Midey, A. J.; Osgood, M.; Wu, J.; Wu, C. *International Journal of Mass Spectrometry* **2010**, *298*, 64.

(22) Clowers, B. H.; Hill, H. H. *Analytical Chemistry* **2005**, *77*, 5877.

(23) Shvartsburg, A. A.; Creese, A. J.; Smith, R. D.; Cooper, H. J. *Analytical Chemistry* **2010**, *82*, 8327.

(24) Zucker, S.; Lee, S.; Webber, N.; Valentine, S.; Reilly, J.; Clemmer, D. *Journal of The American Society for Mass Spectrometry* **2011**, *22*, 1477.

(25) Tang, X.; Bruce, J. E.; Hill, H. H. *Rapid Communications in Mass Spectrometry* **2007**, *21*, 1115.

(26) Croxatto, A.; Prod'hom, G.; Greub, G. *FEMS Microbiology Reviews* **2012**, *36*, 380.

(27) Xia, Y. N.; Yang, P. D.; Sun, Y. G.; Wu, Y. Y.; Mayers, B.; Gates, B.; Yin, Y. D.; Kim, F.; Yan, Y. Q. *Adv. Mater.* **2003**, *15*, 353.

(28) Geim, A. K.; Novoselov, K. S. *Nat. Mater.* **2007**, *6*, 183.

(29) Baughman, R. H.; Zakhidov, A. A.; de Heer, W. A. *Science* **2002**, *297*, 787.

(30) Tasis, D.; Tagmatarchis, N.; Bianco, A.; Prato, M. *Chemical Reviews* **2006**, *106*, 1105.

(31) Odom, T. W.; Huang, J.-L.; Kim, P.; Lieber, C. M. *The Journal of Physical Chemistry B* **2000**, *104*, 2794.

(32) Zhu, Y.; Murali, S.; Cai, W.; Li, X.; Suk, J. W.; Potts, J. R.; Ruoff, R. S. *Advanced Materials* **2010**, *22*, 3906.

(33) Shi Kam, N. W.; Jessop, T. C.; Wender, P. A.; Dai, H. *Journal of the American Chemical Society* **2004**, *126*, 6850.

(34) Prato, M.; Kostarelos, K.; Bianco, A. *Accounts of Chemical Research* **2007**, *41*, 60.

(35) Kam, N. W. S.; O'Connell, M.; Wisdom, J. A.; Dai, H. *Proceedings of the National Academy of Sciences of the United States of America* **2005**, *102*, 11600.

(36) Liu, Z.; Robinson, J. T.; Sun, X.; Dai, H. *Journal of the American Chemical Society* **2008**, *130*, 10876.

(37) Allen, B. L.; Kichambare, P. D.; Star, A. *Advanced Materials* **2007**, *19*, 1439.

(38) Kauffman, D. R.; Star, A. *Chemical Society Reviews* **2008**, *37*, 1197.

(39) Muller, J.; Huaux, F.; Moreau, N.; Misson, P.; Heilier, J.-F.; Delos, M.; Arras, M.; Fonseca, A.; Nagy, J. B.; Lison, D. *Toxicology and Applied Pharmacology* **2005**, *207*, 221.

(40) Shvedova, A. A.; Kisin, E. R.; Mercer, R.; Murray, A. R.; Johnson, V. J.; Potapovich, A. I.; Tyurina, Y. Y.; Gorelik, O.; Arepalli, S.; Schwegler-Berry, D.; Hubbs, A. F.; Antonini, J.; Evans, D. E.; Ku, B.-K.; Ramsey, D.; Maynard, A.; Kagan, V. E.; Castranova, V.; Baron, P. *American Journal of Physiology - Lung Cellular and Molecular Physiology* **2005**, *289*, L698.

(41) Maynard, A. D.; Baron, P. A.; Foley, M.; Shvedova, A. A.; Kisin, E. R.; Castranova, V. *Journal of Toxicology and Environmental Health, Part A* **2004**, *67*, 87.

(42) Clemmer, D. E.; Jarrold, M. F. *Journal of Mass Spectrometry* **1997**, *32*, 577.

(43) Wyttenbach, T.; Kemper, P. R.; Bowers, M. T. *International Journal of Mass Spectrometry* **2001**, *212*, 13.

(44) Koeniger, S. L.; Merenbloom, S. I.; Valentine, S. J.; Jarrold, M. F.; Udseth, H. R.; Smith, R. D.; Clemmer, D. E. *Analytical Chemistry* **2006**, *78*, 4161.

(45) Steiner, W. E.; Clowers, B. H.; Haigh, P. E.; Hill, H. H. *Analytical Chemistry* **2003**, *75*, 6068.

(46) McKnight, L. G.; McAfee, K. B.; Sipler, D. P. *Physical Review* **1967**, *164*, 62.

(47) von Helden, G.; Wyttenbach, T.; Bowers, M. T. *Int. J. Mass Spectrom. Ion Process.* **1995**, *146–147*, 349.

(48) Asbury, G. R.; Hill, H. H. *Analytical Chemistry* **1999**, *72*, 580.

(49) Howdle, M. D.; Eckers, C.; Laures, A. M. F.; Creaser, C. S. *International Journal of Mass Spectrometry* **2010**, *298*, 72.

(50) Tang, K.; Shvartsburg, A. A.; Lee, H.-N.; Prior, D. C.; Buschbach, M. A.; Li, F.; Tolmachev, A. V.; Anderson, G. A.; Smith, R. D. *Analytical Chemistry* **2005**, *77*, 3330.

(51) Clowers, B. H.; Siems, W. F.; Hill, H. H.; Massick, S. M. *Analytical Chemistry* **2005**, *78*, 44.

(52) Kanu, A. B.; Dwivedi, P.; Tam, M.; Matz, L.; Hill, H. H. *Journal of Mass Spectrometry* **2008**, *43*, 1.

(53) Revercomb, H. E.; Mason, E. A. *Analytical Chemistry* **1975**, *47*, 970.

(54) Merenbloom, S. I.; Koeniger, S. L.; Valentine, S. J.; Plasencia, M. D.; Clemmer, D. E. *Anal. Chem.* **2006**, *78*, 2802.

(55) Kemper, P. R.; Dupuis, N. F.; Bowers, M. T. *International Journal of Mass Spectrometry* **2009**, *287*, 46.

(56) Merenbloom, S. I.; Glaskin, R. S.; Henson, Z. B.; Clemmer, D. E. *Anal. Chem. (Washington, DC, U. S.)* **2009**, *81*, 1482.

(57) May, J.; Russell, D. *Journal of The American Society for Mass Spectrometry* **2011**, *22*, 1134.

(58) Merenbloom, S. I.; Koeniger, S. L.; Valentine, S. J.; Plasencia, M. D.; Clemmer, D. E. *Analytical Chemistry* **2006**, *78*, 2802.

(59) Allen, B. L.; Kotchey, G. P.; Chen, Y.; Yanamala, N. V. K.; Klein-Seetharaman, J.; Kagan, V. E.; Star, A. *Journal of the American Chemical Society* **2009**, *131*, 17194.

(60) Kagan, V. E.; Konduru, N. V.; Feng, W.; Allen, B. L.; Conroy, J.; Volkov, Y.; Vlasova, I. I.; Belikova, N. A.; Yanamala, N.; Kapralov, A.; Tyurina, Y. Y.; Shi, J.; Kisin, E. R.; Murray, A. R.; Franks, J.; Stolz, D.; Gou, P.; Klein-Seetharaman, J.; Fadeel, B.; Star, A.; Shvedova, A. A. *Nat Nano* **2010**, *5*, 354.

(61) Kotchey, G. P.; Hasan, S. A.; Kapralov, A. A.; Ha, S. H.; Kim, K.; Shvedova, A. A.; Kagan, V. E.; Star, A. *Accounts of Chemical Research* **2012**, *45*, 1770.

(62) Zhou, X.; Zhang, Y.; Wang, C.; Wu, X.; Yang, Y.; Zheng, B.; Wu, H.; Guo, S.; Zhang, J. *ACS Nano* **2012**, *6*, 6592.

(63) Journet, C.; Maser, W. K.; Bernier, P.; Loiseau, A.; de la Chapelle, M. L.; Lefrant, S.; Deniard, P.; Lee, R.; Fischer, J. E. *Nature* **1997**, *388*, 756.

(64) March, R. E.; Miao, X.-S. *International Journal of Mass Spectrometry* **2004**, *231*, 157.

(65) Lee, S.; Li, Z.; Valentine, S. J.; Zucker, S. M.; Webber, N.; Reilly, J. P.; Clemmer, D. E. *Int. J. Mass Spectrom.* **2012**, *309*, 154.

(66) Rogalewicz, F.; Bourcier, S.; Hoppilliard, Y. *Rapid Communications in Mass Spectrometry* **2005**, *19*, 743.

(67) Liu, R.; Ye, M.; Guo, H.; Bi, K.; Guo, D.-a. *Rapid Communications in Mass Spectrometry* **2005**, *19*, 1557.

(68) Kosynkin, D. V.; Higginbotham, A. L.; Sinitskii, A.; Lomeda, J. R.; Dimiev, A.; Price, B. K.; Tour, J. M. *Nature* **2009**, *458*, 872.

(69) Habicht, S. C.; Vinueza, N. R.; Archibold, E. F.; Duan, P.; Kenttamaa, H. I. *Analytical Chemistry* **2008**, *80*, 3416.

(70) Jeilani, Y. A.; Cardelino, B. H.; Ibeanusi, V. M. *Journal of Mass Spectrometry* **2010**, *45*, 678.

(71) Earls, A. O.; Axford, I. P.; Braybrook, J. H. *Journal of Chromatography A* **2003**, *983*, 237.

(72) Silva, P. J.; Prather, K. A. *Analytical Chemistry* **2000**, *72*, 3553.

(73) Kamrin, M. A. *Journal of Toxicology and Environmental Health, Part B* **2009**, *12*, 157.

(74) Weber, R. J. M.; Li, E.; Bruty, J.; He, S.; Viant, M. R. *Bioinformatics* **2012**, *28*, 2856.

(75) Sowell, R. A.; Koeniger, S. L.; Valentine, S. J.; Moon, M. H.; Clemmer, D. E. *J. Am. Soc. Mass Spectrom.* **2004**, *15*, 1341.